Geochemical Perspectives Letters

Zircon growth experiments reveal limited equilibrium Zr isotope fractionation in magmas

H.G.D. Tompkins[1], M. Ibañez-Mejia[1*], F.L.H. Tissot[2], E. Bloch[3], Y. Wang[1,4], D. Trail[4]

https://doi.org/10.7185/geochemlet.2310

Abstract

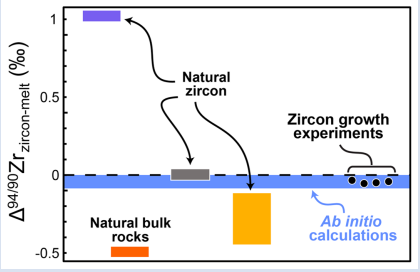

Recent studies of zirconium isotopes in igneous systems have revealed significant mass dependent variability, the origin of which remains intensely debated. While magmatic zircon crystallisation could potentially drive equilibrium isotope fractionation, given that Zr^{4+} undergoes a shift in coordination as zircon precipitates from a silicic melt, *ab initio* calculations predict only limited equilibrium fractionation between zircon and melt at magmatic temperatures. To resolve this debate, we determined the isotopic fractionation between co-existing zircon and silicic melt using controlled zircon growth experiments. Our experimental results indicate that zircon has a lower $\delta^{94/90}Zr$ relative to co-existing melt by ~0.045 ‰ at magmatic conditions, which is in excellent agreement with *ab initio* predictions. Our results imply that, for most natural systems studied to date, the observed variability is predominantly a result of non-equilibrium rather than equilibrium isotope fractionation during zircon crystallisation.

Received 27 October 2022 | Accepted 1 March 2023 | Published 28 March 2023

Introduction

Zirconium (Zr) belongs to a group of transition metals known as the high field strength elements, which due to their distinctive geochemical properties are used to trace magmatic differentiation and the co-evolution of Earth's mantle and crust. While studies of Zr stable isotope variation (expressed as $\delta^{94/90}Zr = [(^{94}Zr/^{90}Zr)_{Sample}/(^{94}Zr/^{90}Zr)_{Standard} - 1]\cdot1000$) have all linked Zr isotopic variability to zircon crystallisation during magmatic differentiation, they have also yielded conflicting observations regarding the direction and magnitude of Zr isotope fractionation in magmatic systems. Based on a $\delta^{94/90}Zr$ *vs.* SiO_2 trend in volcanic rocks from Hekla, Iceland, Inglis *et al.* (2019) suggested zircon is isotopically light compared to coexisting melt, and inferred a fractionation factor $\Delta^{94/90}Zr_{zircon\text{-}melt}$ (*i.e.* $\approx1000\cdot\ln(\alpha_{zircon\text{-}melt})$, where $\alpha_{zircon\text{-}melt} = [(^{94}Zr/^{90}Zr)_{Zircon}/(^{94}Zr/^{90}Zr)_{Melt}]$) of −0.5 ‰. Conversely, through measurement of single zircon and baddeleyite crystals from a gabbroic cumulate, Ibañez-Mejia and Tissot (2019) found these phases to be isotopically heavy relative to the starting melt using the bulk rock $\delta^{94/90}Zr$ as a proxy, and inferred a $\Delta^{94/90}Zr_{zircon\text{-}melt} = 1.06$ ‰. A subsequent study by Guo *et al.* (2020) observed internally zoned zircon with isotopically light cores and progressively heavier rims, which they interpreted as equilibrium Rayleigh fractionation of isotopically light zircon from a melt with $\Delta^{94/90}Zr_{zircon\text{-}melt}$ between −0.12 and −0.45 ‰. However, in all studies conducted to date on natural samples, no co-existing zircon-glass pairs have been directly measured. Rather, zircon-melt fractionation factors have only been inferred by calculation (*e.g.*, Rayleigh fitting or mass balance considerations).

Adding to this conundrum, no resolvable $\delta^{94/90}Zr$ variations (and therefore negligible fractionation) have been observed in several reference zircons (*e.g.*, 91500, Mud Tank, and Plešovice; Tompkins *et al.*, 2020; Zhang *et al.*, 2019), and recent *ab initio* calculations by Chen *et al.* (2020) and Méheut *et al.* (2021) predict that the magnitude of equilibrium Zr isotope fractionation at magmatic temperatures is too small ($\Delta^{94/90}Zr_{zircon\text{-}melt} \leq 0.08$ ‰) to explain the large fractionations observed in natural systems. Instead, both theoretical studies concluded that a combination of equilibrium and kinetic fractionation processes during crystallisation of zircon and rock forming minerals is necessary to produce the large variations observed in natural igneous systems.

Here, we address these conflicting observations from an experimental standpoint. Using zircon growth experiments performed under controlled laboratory conditions, we sought to determine the isotopic fractionation factor between zircon and melt ($\Delta^{94/90}Zr_{zircon\text{-}melt}$; hereafter $\Delta^{94/90}Zr$ for brevity) at various temperatures and melt compositions. To do so, experimental zircon and co-existing melts (quenched to a glass) were: 1) chemically separated using a novel sequential acid leaching procedure, and 2) their $\delta^{94/90}Zr$ were measured at high accuracy and precision using a ^{91}Zr-^{96}Zr double spike method.

1. Department of Geosciences, The University of Arizona, Tucson, AZ 85721, United States
2. The Isotoparium, Division of Geological and Planetary Sciences, California Institute of Technology, Pasadena, CA 91125, United States
3. School of Geosciences and the Environment, University of Lausanne, Lausanne, Switzerland
4. Department of Earth and Environmental Sciences, University of Rochester, Rochester, NY 14627, United States
* Corresponding author (email: ibanezm@arizona.edu)

Experimental Procedure and Samples

We utilised run products from zircon growth experiments performed by Wang and Trail (2019) and analysed: i) 11 experimental products published in Wang and Trail (2019), ii) three 'low temperature' (925 °C) experiments also performed by Wang and Trail (2019) but previously unpublished because they produced zircon crystals too small for that study, and iii) homogenised fractions of four starting base mixes that represent the starting composition (*i.e.* bulk system) for all experiments. Zircon growth experiments were performed in a piston cylinder apparatus at various temperatures and melt compositions (Table S-1). Various synthetic mixtures (dubbed 'base mixes') were prepared to simulate a range of hydrous felsic melts in the SiO_2-Al_2O_3-Na_2O-K_2O-CaO-ZrO_2-H_2O system with H_2O fixed at ~10 wt. % and doped with 500 ppm rubidium (Rb). Because Rb is highly incompatible in zircon, this trace element served as monitor for melt incorporation in the laser ablation study of Wang and Trail (2019), and was used as proxy for zircon-melt chemical separation in this study (see Supplementary Information). The base mixes covered a range of aluminum saturation indices (ASI = molar ratio of $Al_2O_3/[CaO + Na_2O + K_2O]$) alkalinity indices (A/NK = molar ratio of $Al_2O_3/[Na_2O + K_2O]$) and M factors (M = molar ratio of $[K + Na + 2Ca]/[Si \times Al]$), as these are useful criteria for characterising felsic rocks and parameterising zircon saturation in silicate melts (*e.g.*, Boehnke *et al.*, 2013). Further details about the experiments and run products can be found in Wang and Trail (2019).

The experiments studied here cover a wide range of temperatures (1400 °C to 925 °C), ASI (0.9 to 1.3), A/NK (1.4 to 2.2) and M parameters (1.2 to 1.8) (Table S-1). In all cases, the experimental products consisted of a mixture of glass (quenched melt) and zircon. Since the zircon crystals in all experiments are too small (mostly ≤20 μm in diameter) to physically separate from the glass, we designed an extraction procedure using sequential acid leaching to attain full chemical separation of these phases. Our calibrated protocol resulted in complete separation of glass from zircon, enabling each fraction to be independently spiked and prepared for isotopic analysis. Once separation was achieved, all fractions were measured for their $\delta^{94/90}$Zr relative to the NIST standard using the analytical methods described in Tompkins *et al.* (2020). Analytical methods are summarised in the Supplementary Information.

For each experimental product, we determined the total mass fraction of Zr removed from the liquid in the form of zircon relative to the bulk initial (*i.e.* f factor). Mean f values and their variability within the liquid at the time of quenching were determined *in situ* using Zr concentration measurements in glass fragments *via* secondary ion mass spectrometry (SIMS). The mean and variability in f values assigned in this manner were used to propagate uncertainties through all subsequent calculations. To ensure consistency, the mean f values determined using SIMS measurements of glass were verified using Zr/Rb measurements from solutions produced after acid leaching of glasses during preparation for isotopic analyses. Details about methods and calculations are included in the Supplementary Information.

Results

Results from all our measurements are reported in Tables S-2, S-3, and shown graphically in Figure 1. Experiments were found to yield mean f values between 0.12 ± 0.06 and 0.97 ± 0.01. The $\delta^{94/90}$Zr of the four base mixes were undistinguishable within uncertainty, and their mean value (0.054 ± 0.005 ‰) is depicted in Figure 1a (horizontal grey band). Results for all 14 zircon-glass pairs analysed are shown ranked by increasing mean f. All zircon fractions exhibit lower $\delta^{94/90}$Zr with respect to the bulk system, ranging from −0.168 ± 0.011 ‰ to −0.068 ± 0.013 ‰. In contrast, glasses have a bimodal $\delta^{94/90}$Zr distribution; six high temperature (1300 – 1400 °C) experiments yielded mean $f \leq 0.53$ and glass $\delta^{94/90}$Zr values indistinguishable from the bulk system within uncertainty (−0.057 ± 0.016 ‰ to −0.050 ± 0.013 ‰), while the eight experiments conducted at lower temperatures (925 – 1150 °C) yielded mean $f \geq 0.78$ and positive glass $\delta^{94/90}$Zr values (−0.004 ± 0.013 ‰ to +0.123 ± 0.013 ‰) compared to the bulk. Isotopic mixing calculations performed using the $\delta^{94/90}$Zr and f determined for each glass-zircon pair show excellent agreement within uncertainty with respect to the $\delta^{94/90}$Zr value of the starting base mix, thus confirming mass balance (Fig. 1b).

Discussion

The diffusivity of Zr^{4+} in zircon is expected to be extremely low even at magmatic temperatures (Cherniak *et al.*, 1997; Ibañez-Mejia and Tissot, 2019). Therefore, the growth of zircon from a magma removes Zr as a Rayleigh-type process even if chemical and isotopic equilibrium partitioning between the solid and melt are maintained, where only the outermost rim of the crystal is in equilibrium with the immediately surrounding melt while interior domains of the zircon become isolated from the rest of the system (Criss, 1999). In an equilibrium Rayleigh scenario, one could directly recover $\Delta^{94/90}$Zr from experiments by measuring the isotopic composition of the outermost zircon rim and melt in direct equilibrium, but this is impossible to achieve using our experimental setup. Instead, our chemical separation method produces bulk glass and bulk (*i.e.* cumulative) zircon fractions, meaning that we can only capture the total integrated isotopic effects that a Rayleigh-type process imposes on $\delta^{94/90}$Zr over the entire f interval of the experiment.

To approximate $\Delta^{94/90}$Zr using the results of Figure 1a, we took an inverse approach that treats each zircon crystallisation experiment as an equilibrium Rayleigh fractionation. The recovered $\Delta^{94/90}$Zr are summarised in Figure 1c, where they are compared with theoretically predicted values at 1300 – 700 °C from *ab initio* calculations. While all but one of our experiments conform to mass balance (Fig. 1b), for most high T experiments (low f) the $\delta^{94/90}$Zr of the zircon, glass, and bulk system could not all be exactly fitted using an equilibrium Rayleigh fractionation inversion. For experiments where $f \leq 0.53$, zircon fractions have $\delta^{94/90}$Zr values that are 'too low' for their respective mean f if an *equilibrium* process is assumed. For these experiments, we used the absolute difference in $\delta^{94/90}$Zr between the glass and bulk zircon measurements (a parameter we refer to as $\Delta^{94/90}Zr_{apparent}$), as a *maximum* permissible limit for the $\Delta^{94/90}$Zr governing that experiment (see Supplementary Information for a detailed rationale of this approach).

In general, all of the $\Delta^{94/90}Zr_{apparent}$ values determined from high T (low f) experiments, as well as the best fit $\Delta^{94/90}$Zr values from Rayleigh inversion of low T (high f) experiments, indicate that: i) zircon is invariably isotopically light relative to the melt from which it precipitates, and ii) that the magnitude of the fractionation factor between zircon and melt ($\Delta^{94/90}$Zr) is always smaller than −0.139 ‰ over the experimental temperature range. Details of the mathematical approach and parameters used to estimate $\Delta^{94/90}$Zr and calculate uncertainties are included in the Supplementary Information.

To explore whether temperature and/or melt compositional differences are controlling the variable fractionations observed between experiments, Figure 2 shows the fractionation

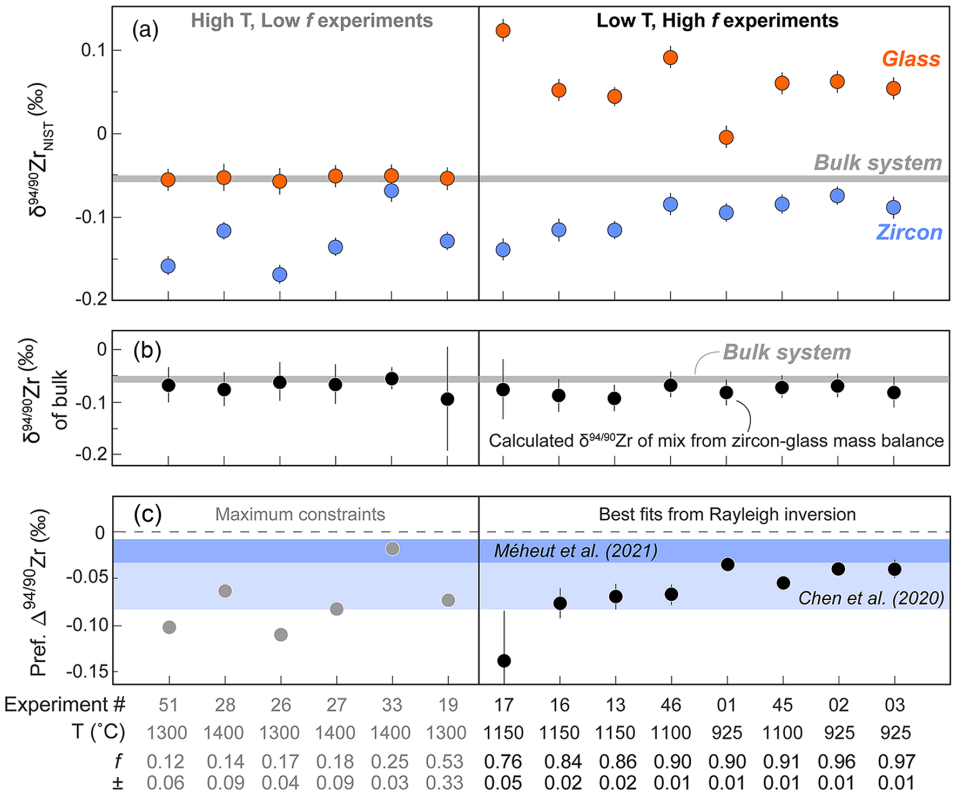

Figure 1 **(a)** $\delta^{94/90}$Zr of the glass (orange) and bulk zircon (blue) for each experiment. 'Bulk system' is the mean value of all experimental base mixes. **(b)** Mass balance calculations for all glass-zircon pairs compared to the $\delta^{94/90}$Zr of the bulk starting mix. **(c)** Apparent $\Delta^{94/90}$Zr, the fractionation factor between zircon and melt, determined for each experiment (see text for further details and discussion). Range of *ab initio* values between 1300 °C and 700 °C (Chen *et al.*, 2020; Méheut *et al.*, 2021) are shown as horizontal blue bands. Samples are shown rank ordered by increasing mean *f*. Uncertainties, visible only when larger than the symbols, are 2σ.

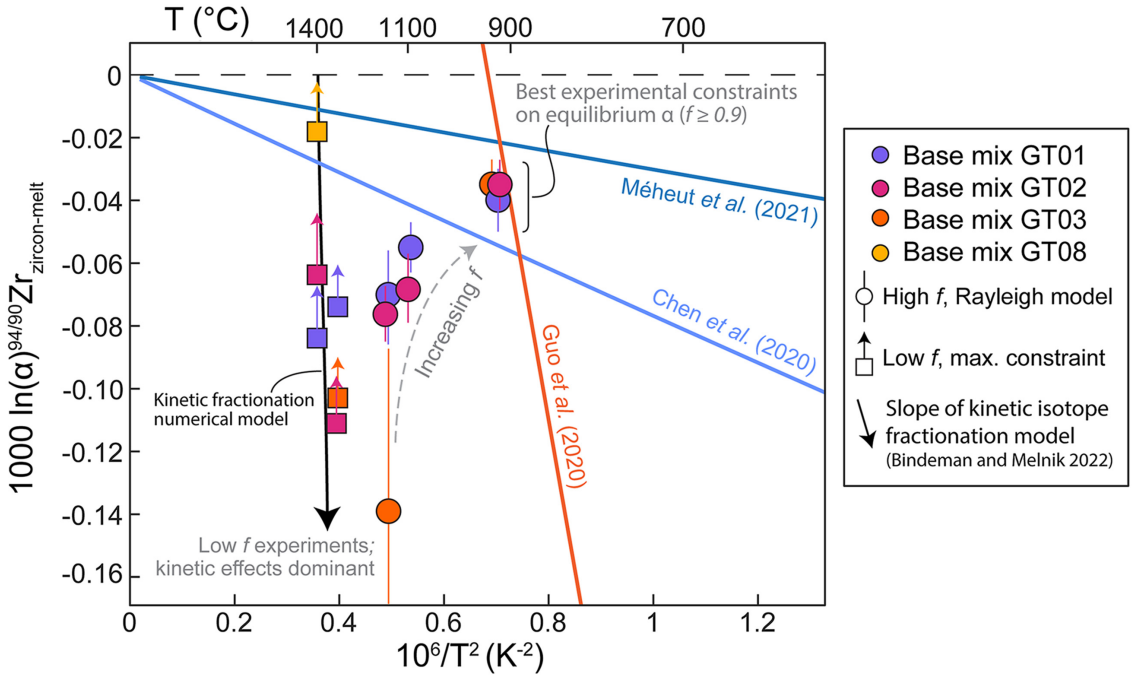

Figure 2 Temperature dependence of zircon-melt fractionation factors from *ab initio* studies (Chen *et al.*, 2020; Méheut *et al.*, 2021), natural samples (Guo *et al.*, 2020), and our experiments. Circles are low T, high *f* experiments in Figure 1, from which $\Delta^{94/90}$Zr was retrieved using Rayleigh inversion. Squares denote high T, low *f* experiments, where only a *maximum* magnitude for fractionation ($\Delta^{94/90}Zr_{apparent}$) in that experiment could be constrained (see text). Black solid line is the slope of kinetic isotope fractionation during diffusion limited growth of a zircon nucleating at 1400 °C, calculated using the numerical code of Bindeman and Melnik (2022) (see Supplementary Information for details).

results of Figure 1c plotted as a function of their inverse squared temperature. The *ab initio* zircon fractionation models of Chen *et al.* (2020) (relative to Ca-catapleiite) and Meheut *et al.* (2021) (relative to gittinsite) are shown for comparison, as well as the model of Guo *et al.* (2020), obtained from Rayleigh inversion of $\delta^{94/90}$Zr zoning in natural zircon. It is important to note, however, that because the Guo *et al.* (2020) model does not result in a $\Delta^{94/90}Zr = 0$ at infinite temperature (*i.e.* $1/T^2 = 0$), it has little physical meaning and, unlike as argued in that study, cannot represent an equilibrium fractionation process (Schauble *et al.*, 2009; Young *et al.*, 2015).

Close inspection of Figure 2 reveals that our data do not plot along a single slope in $\Delta^{94/90}$Zr *vs.* $1/T^2$ space, which clearly indicates that effects other than equilibrium isotope partitioning are influencing the $\Delta^{94/90}$Zr values calculated from our experiments. Because no arrays that are co-linear with the origin of this plot are defined among experiments sharing any given base mix, the scatter is unlikely to be caused by a melt chemistry dependence (*e.g.*, variable M, ASI or A/NK) of the fractionation factor. Our high T experiments exhibit the largest $\Delta^{94/90}$Zr scatter at any given T and define a steep array with a slope indicative of non-equilibrium fractionation.

Non-equilibrium trace element and isotope partitioning is expected to develop in solids growing from a magma when the distribution coefficient ($K_D = [i]_{solid}/[i]_{liquid}$) of a species of interest [*i*] diverges from unity, with the magnitude of the effects increasing proportionally to the ratio of phase boundary migration velocity over the diffusivity of the species in question (Albarede and Bottinga, 1972; Watson and Müller, 2009; Watkins *et al.*, 2017). Although analytical expressions to quantify this process in radial coordinates exist (*e.g.*, Eq. 11 of Watson and Müller, 2009), these are not applicable to the case of zircon growth as the conditions for this process are outside the bounds over which the Watson and Müller (2009) relationships are accurate (*i.e.* these apply for trace species where $K_D < \approx 0.5$). Thus, at present, the magnitude of Zr isotope fractionation during diffusion limited growth of magmatic zircon is better approached numerically.

To test for a possible kinetic control on isotope fractionation in our experiments, we used the numerical approach of Bindeman and Melnik (2022) to calculate an expected $\Delta^{94/90}$Zr *vs.* $1/T^2$ relation for zircon nucleating at 1400 °C and using model parameters close to those of our experimental conditions (see Supplementary Information). Because β factors (an empirical parameter describing the efficiency of diffusive isotope fractionation; Richter *et al.*, 1999) for Zr in melt have not yet been determined, we do not attempt to reproduce our experiments quantitatively. However, it can be clearly seen from Figure 2 that the slope of kinetic isotope fractionation in $\Delta^{94/90}$Zr *vs.* $1/T^2$ space closely resembles the trend defined by our high T experiments, and is also similar to the slope of the Guo *et al.* (2020) model defined using natural zircon nucleated at lower temperatures. Thus, we interpret these steep arrays that do not intersect the origin of a $\Delta^{94/90}$Zr *vs.* $1/T^2$ plot as reflecting a combination of equilibrium and kinetic isotope fractionation effects, resulting in a compounded, larger fractionation than what can be imparted by vibrational equilibrium processes alone. Nevertheless, because β factors for Zr remain unknown, quantitative deconvolution of kinetic and equilibrium fractionation contributions to natural and experimental $\Delta^{94/90}$Zr data is not yet possible.

Given the above observations, we consider the experiments performed at high T (low *f*) inadequate for quantifying an equilibrium fractionation coefficient, and instead argue that the results from our highest *f* experiments ($n = 4$ where $f \geq 0.9$)) yield the $\Delta^{94/90}$Zr that *most closely approach* the magnitude of the equilibrium fractionation factor. Indeed, isotope effects recorded by a solid growing in a kinetically dominated system where $K_D >> 1$ are significant at low *f* (*e.g.*, Fig. 12 of Watson and Müller, 2009), whereas the impact of kinetic fractionation on the *cumulative* solid composition must, by mass balance, approach zero as *f* tends to unity. Results from experiments where $f \geq 0.9$ yield a mean $\Delta^{94/90}$Zr of −0.045 ‰. Although these experiments can potentially also be affected to some small degree by kinetic isotope effects, they all tightly cluster between the $\Delta^{94/90}$Zr models of Chen *et al.* (2020) and Méheut *et al.* (2021) (Fig. 2), supporting the accuracy of these first principles calculations. While our results cannot distinguish which of these two theoretical models is more accurate, we note that the absolute difference in $\Delta^{94/90}$Zr at magmatic T between these studies is exceedingly small. As such, our results experimentally confirm their predictions, and reinforce the notion that large fractionations observed in natural zircon cannot be the result of equilibrium fractionation processes.

Overall, our results are in excellent agreement with the direction of isotopic fractionation estimated from *ab initio* studies and, for our lowest T experiments ($f \geq 0.9$), also its magnitude. Our results thus confirm that the expected effects of equilibrium isotope fractionation during magmatic zircon crystallisation are

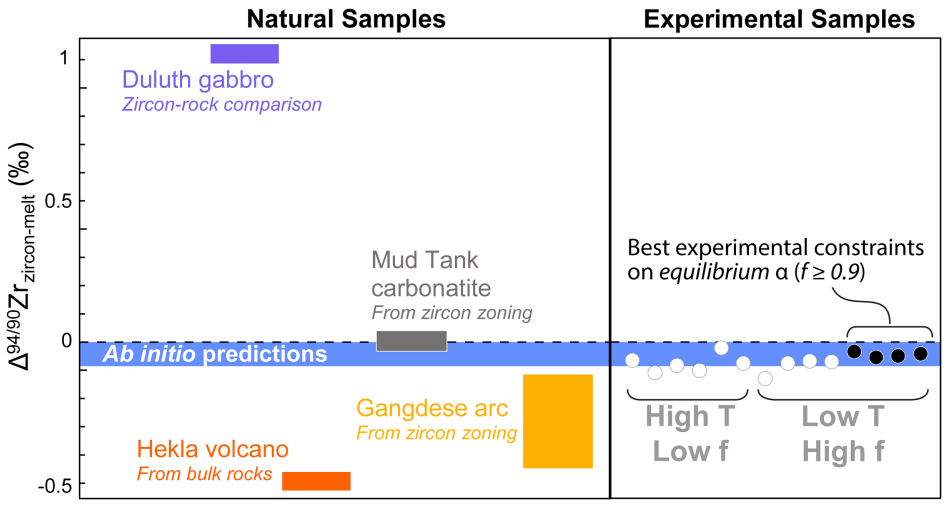

Figure 3 Summary of zircon-melt fractionation factors from *ab initio* calculations at ≥700 °C (Chen *et al.*, 2020; Méheut *et al.*, 2021), natural samples (Ibañez-Mejia and Tissot, 2019; Inglis *et al.*, 2019; Guo *et al.*, 2020; Tompkins *et al.*, 2020), and experimental samples (this study).

exceedingly small, demonstrating that the observed range of natural variability cannot be explained by this mechanism (Fig. 3). Instead, and as argued by Chen *et al.* (2020), Méheut *et al.* (2021), and Tissot and Ibañez-Mejia (2021), we conclude that non-equilibrium effects are needed to explain, and must be the dominant driver of, the large Zr isotope variations observed in natural systems.

Conclusions and Implications

This study demonstrates that: 1) at equilibrium, zircon is isotopically light compared to its co-existing silicic melt; 2) the magnitude of equilibrium Zr isotope fractionation between zircon and melt at magmatic temperatures is extremely small ($\Delta^{94/90}Zr \approx -0.045$ ‰), as predicted by *ab initio* calculations; and 3) the large $\delta^{94/90}Zr$ variations observed in natural igneous systems to date are not the result of equilibrium fractionation during zircon crystallisation. Our results reinforce the notion that kinetic isotope effects play a central, if not the dominant, role in fractionating Zr isotopes in high temperature environments. Thus, additional experimental constraints that quantify the magnitude of kinetic separation of Zr isotopes in solids and liquids (*e.g.*, Watkins *et al.*, 2017) are needed before the fractionations observed in natural systems can be fully understood and quantified.

Acknowledgements

This project was supported by NSF Graduate Research Fellowship award DGE-1746060, an MSA Student Research Grant, and a GSA Student Research Grant (to HGDT), as well as NSF-EAR grants 2131632 and 2143168 (to MIM), 1824002 (to FLHT), 1650033 (to DT), and SNSF Ambizione grant PZ00P2_173988 (to EB). FLHT acknowledges additional support from NSF grant MGG-2054892, a Packard Fellowship, a research award from the Heritage Medical Research Institute, and startup funds from Caltech. The authors thank editor Anat Shahar, James Van Orman, and an anonymous reviewer, for constructive reviews that improved the clarity of this article.

Editor: Anat Shahar

Additional Information

Supplementary Information accompanies this letter at https://www.geochemicalperspectivesletters.org/article2310.

Cite this letter as: Tompkins, H.G.D, Ibañez-Mejia, M., Tissot, F.L.H, Bloch, E., Wang, Y., Trail, D. (2023) Zircon growth experiments reveal limited equilibrium Zr isotope fractionation in magmas. *Geochem. Persp. Let.* 25, 25–29. https://doi.org/10.7185/geochemlet.2310

References

Albarede, F. and Bottinga, Y. (1972) Kinetic disequilibrium in trace element partitioning between phenocrysts and host lava. *Geochimica Cosmochimica Acta* 36, 141–156. https://doi.org/10.1016/0016-7037(72)90003-8

Bindeman, I.N. and Melnik, O.E. (2022) The rises and falls of zirconium isotopes during zircon crystallisation. *Geochemical Perspectives Letters* 24, 17–21. https://doi.org/10.7185/geochemlet.2241

Boehnke, P., Watson, E.B., Trail, D., Harrison, T.M., and Schmitt, A.K. (2013) Zircon saturation re-revisited. *Chemical Geology* 351, 324–334. https://doi.org/10.1016/j.chemgeo.2013.05.028

Chen, X., Wang, W., Zhang, Z., Nie, N.X., and Dauphas, N. (2020) Evidence from *Ab Initio* and Transport Modeling for Diffusion-Driven Zirconium Isotopic Fractionation in Igneous Rocks. *ACS Earth and Space Chemistry* 4, 1572–1595. https://doi.org/10.1021/acsearthspacechem.0c00146

Cherniak, D.J., Hanchar, J.M., and Watson, E.B. (1997) Diffusion of tetravalent cations in zircon. *Contributions to Mineralogy and Petrology* 127, 383–390. https://doi.org/10.1007/s004100050287

Criss, R.E. (1999) *Principles of Stable Isotope Distribution*. Oxford Univ Press, New York. https://doi.org/10.1093/oso/9780195117752.001.0001

Guo, J.L. Wang, Z., Zhang, W., Moynier, F., Cui, D., Hu, Z., Ducea, M. (2020) Significant Zr isotope variations in single zircon grains recording magma evolution history. *Proceedings of the National Academy of Sciences* 117, 21125–21131. https://doi.org/10.1073/pnas.2002053117

Ibañez-Mejia, M., and Tissot, F.L.H. (2019) Extreme Zr stable isotope fractionation during magmatic fractional crystallization. *Science Advances* 5, eaax8648. https://doi.org/10.1126/sciadv.aax8648

Inglis, E.C., Moynier, F., Creech, J., Deng, Z., Day, J.M.D., Teng, F.Z., Bizzarro, M., Jackson, M., and Savage, P. (2019) Isotopic fractionation of zirconium during magmatic differentiation and the stable isotope composition of the silicate Earth. *Geochimica Cosmochimica Acta* 250, 311–323. https://doi.org/10.1016/j.gca.2019.02.010

Méheut, M., Ibañez-Mejia, M., and Tissot, F.L.H. (2021) Drivers of zirconium isotope fractionation in Zr-bearing phases and melts: The roles of vibrational, nuclear field shift and diffusive effects. *Geochimica Cosmochimica Acta* 292, 217–234. https://doi.org/10.1016/j.gca.2020.09.028

Richter, F.M., Liang, Y., and Davis, A.M. (1999) Isotope fractionation by diffusion in molten oxides. *Geochimica Cosmochimica Acta* 63, 2853–2861. https://doi.org/10.1016/S0016-7037(99)00164-7

Schauble, E.A., Méheut, M., and Hill, P.S. (2009) Combining Metal Stable Isotope Fractionation Theory with Experiments. *Elements* 5, 369–374. https://doi.org/10.2113/gselements.5.6.369

Tissot, F.L.H., and Ibañez-Mejia, M. (2021) Unlocking the single-crystal record of heavy stable isotopes. *Elements* 17 (6), 389–394. https://doi.org/10.2138/gselements.17.6.389

Tompkins, H.G.D., Zieman, L.J., Ibañez-Mejia, M., and Tissot, F.L.H. (2020) Zirconium stable isotope analysis of zircon by MC-ICP-MS: Methods and application to evaluating intra-crystalline zonation in a zircon megacryst. *Journal of Analytical Atomic Spectrometry* 35, 1167–1186. https://doi.org/10.1039/C9JA00315K

Wang, Y., and Trail, D. (2019) Aluminum partitioning between zircon and haplogranitic melts: The influence of temperature and melt composition. *Chemical Geology* 511, 71–80. https://doi.org/10.1016/j.chemgeo.2019.02.016

Watkins, J.M., DePaolo, D.J., and Watson, E.B. (2017) Kinetic fractionation of non-traditional stable isotopes by diffusion and crystal growth reactions. *Reviews in Mineralogy and Geochemistry* 82, 85–125. https://doi.org/10.2138/rmg.2017.82.4

Watson, E.B., and Müller, T. (2009) Non-equilibrium isotopic and elemental fractionation during diffusion-controlled crystal growth under static and dynamic conditions. *Chemical Geology* 267, 111–124. https://doi.org/10.1016/j.chemgeo.2008.10.036

Young, E.D., Manning, C.E., Schauble, E.A., Shahar, A., Macris, C.A., Lazar, C., and Jordan, M. (2015) High-temperature equilibrium isotope fractionation of non-traditional stable isotopes: Experiments, theory, and applications. *Chemical Geology 395*, 176–195. https://doi.org/10.1016/j.chemgeo.2014.12.013

Zhang, W., Wang, Z., Moynier, F., Inglis, E., Tian, S., Li, M., Liu, Y., and Hu, Z. (2019) Determination of Zr isotopic ratios in zircons using laser-Ablation multiple-collector inductively coupled-plasma mass-spectrometry. *Journal of Analytical Atomic Spectrometry 34*, 1800–1809. https://doi.org/10.1039/C9JA00192A

Zircon growth experiments reveal limited equilibrium Zr isotope fractionation in magmas

H.G.D. Tompkins, M. Ibañez-Mejia, F.L.H. Tissot, E. Bloch, Y. Wang, and D. Trail

Supplementary Information

The Supplementary Information includes:

- Methods
- Zircon Isotope Data Processing and Modelling Approach
- Supplementary Tables S-1 to S-5
- Figures S-1 to S-6
- Supplementary Information References

Methods

Processing of Experimental Products

Molybdenum (Mo) – Platinum (Pt) experimental capsules from the study of Wang and Trail (2019) were marked and sliced in half using a sagittal cut with a wire-saw. Only one half of each experimental product was used for this study and the other half was preserved. Capsules were first bathed in 100 ml of concentrated aqua regia for ~72 hours in glass beakers to fully dissolve the Mo outer sleeves surrounding the Pt capsules. Once the Mo sleeve had fully dissolved, the remaining Pt capsules were rinsed multiple times with distilled H_2O and sonicated in 2 % HNO_3 for 30 minutes to ensure all aqua regia and Mo contamination was removed. Without the Mo outer sleeves, the experimental products were easily freed from the thin inner Pt capsules by bending them with a finger. The resulting glass and zircon mixtures were mechanically broken and two small fragments from each run were picked and mounted in epoxy for Secondary Ion Mass Spectrometry (SIMS). The remaining material for each experiment was ground manually under ethanol for 5 minutes using an ultra-high purity corundum mortar and pestle, which had been pre-cleaned twice before processing each experiment by grinding ultra-high-purity silica sand (>99.995% purity) obtained from AdValue Technology. Once reduced to a fine powder, samples were transferred into a pre-cleaned glass beaker by pipetting the ethanol-powder slurry before bringing them into the clean laboratory. The remaining steps were performed inside a Class 1000 clean laboratory supplied with HEPA-filtered air, and inside ULPA-filtered vertical laminar flow hoods that provide a local environment better than Class 100 and closer to Class 10. Samples were transferred into pre-cleaned 7 ml Teflon beakers in 500 µl ethanol and an additional 5 ml of MQ-H_2O were added to dilute the alcohol. Teflon beakers were left uncapped on a hot plate at 70 °C overnight to drive off the alcohol and H_2O was evaporated until only ~100 µl of liquid remained.

Chemical Separation

Because the small (≤20 µm) zircon produced by our experiments cannot be physically separated from the glass, a chemical separation procedure using a series of stepwise leaches was developed. Leaching steps, designed and calibrated to efficiently remove the glass while leaving zircon unreacted, were performed using

3.5 M HNO_3 and variable HF concentration. Figure S-1 shows the results of our final calibration run, where an experimental zircon-glass mixture was subjected to multiple low pressure (*i.e.*, capped beaker in a hot plate at room pressure) acid attack steps with variable HF concentration increasing from 0.1 to 28 M. Because the starting mix was doped with rubidium (Rb), a highly incompatible element in the zircon structure (Thomas *et al.*, 2002), the Rb concentration of each step was used to monitor glass removal and the quality of the chemical separation. As shown in Figure S-1, all Rb was extracted during the first two leaching steps using 0.1 and 0.2 M HF at low pressure, indicating complete glass dissolution at low HF molarities while leaving zircon completely unreacted. No Zr release above instrumental background was observed in any subsequent low-pressure steps ranging from 0.5 to 28 M HF, and Zr from zircon was only extracted after performing a high-pressure dissolution step using a Parr digestion vessel and 28 M HF for 72 hours at 215 ˚C.

Once calibrated, our final protocol consisted of only five low-pressure leaching steps (*i.e.*, 3.5 M HNO_3 + 0.1 M HF, 3.5 M HNO_3 + 0.2 M HF, 3.5 M HNO_3 + 0.75 M HF, 3.5 M HNO_3 + 1.5 M HF, and 15 M HF). The first three leaching steps (glass cut) were combined in a 30 ml Teflon beaker. The 1.5 M and 15 M HF steps were collected separately for concentration measurements of Rb and Zr to verify that glass had been completely removed during the first three leaching steps and that zircon was not being attacked. All concentrations were measured using a quadrupole – inductively coupled plasma - mass spectrometer (Q-ICP-MS) in the Trail lab at University of Rochester. Rb and Zr counts were below the detection limit in all (1.5+15) M HF leaching solutions, confirming that our protocol achieved complete dissolution of glass and complete glass-zircon separation over the first three leaching steps. After confirmation that all glass had been removed, 3 ml of 28 M HF + 1 drop 16 M HNO_3 was added to the beakers, and these were loaded inside a 125 ml high-pressure Parr® vessel. Complete digestion was achieved after ~72 hours at 215 ˚C.

In addition to the zircon-glass experimental products, four bulk starting materials (base mixes) from which the experiments were synthesized were also dissolved for Zr isotope measurements. Approximately 10 mg of these homogenized synthetic powders were loaded into 7 ml Teflon beakers with 3 ml of 28 M HF + 1 drop 16 M HNO_3. Beakers were then loaded inside a high-pressure Parr® vessel for 48 hours at 215 ˚C. Ca-fluoride salts that formed after digestion of base mixes using concentrated HF were completely removed using repeated dry-down and re-digestion steps with 3 M HNO_3 + 0.4 M H_3BO_3, by preferential production and evaporation of volatile BF_3

Spiking and Chromatographic Purification of Zr

Once all zircon, glass, and bulk base mixes were fully in solution, the Zr concentration of all fractions were measured by Q-ICP-MS using gravimetrically prepared calibration standards to ensure accurate spiking. Following concentration measurements, aliquots containing ~495 ng of sample Zr were transferred into clean 7 ml Teflon beakers and mixed with ~405 ng of Zr from a calibrated ^{91}Zr-^{96}Zr DS to achieve an optimal spiking ratio (*i.e.*, 0.45 spike: 0.55 sample; Tompkins *et al.*, 2020). To achieve sample-spike equilibration, samples were fluxed in a capped beaker at 130 ˚C on a hot plate overnight, dried down completely, redigested in 1 ml of 16 M HNO_3, fluxed overnight, and dried down a second time. Samples were then re-digested using 5 ml of a 3 M HNO_3–0.4 M H_3BO_3 mixture for chromatographic purification.

Zirconium was chemically purified by ion-exchange chromatography using the methods described in Tompkins *et al.* (2020). In brief, Zr and Hf were first separated from major elements using 2 ml Eichrom TODGA resin (Pourmand and Dauphas, 2010; Ibañez-Mejia and Tissot, 2019). A "matrix clean-up" step was then performed using Bio-Rad AG1-X8 columns (150 µl volume) to ensure complete removal of Fe and other major elements. Subsequently, Zr was separated from Hf using Eichrom Ln-spec resin, and from Mo and Ru, which are isobaric interferences on several Zr isotopes, using a final clean-up step with AG1-X8 resin. This procedure resulted in total procedural Zr yields >90% and total Mo/Zr < $4x10^{-4}$. Three total procedural blanks (spiked with ca. 60 ng of Zr DS) were processed and measured during this study. All blanks yielded <1 ng

total Zr, which is three orders of magnitude smaller than the amount of sample Zr utilized for each measurement and thus considered negligible. More details on the chemical purification procedures are provided in Tompkins *et al*. (2020) and Klaver *et al.* (2021).

Purified Zr solutions were dried completely and then fluxed in 1 ml 16 M HNO_3 + 1 ml 15 wt. % H_2O_2 for several hours to drive off any remaining organics from the resins. Samples were fully dried again, then taken up in 1 ml 16 M HNO_3 + 0.5 ml 28 M HF in caped beakers to re-digest, and gently dried down to a small bead before taking up ~3 ml of 0.59 M HNO_3 + 0.28 M HF. After fluxing overnight in capped beakers at 100 ˚C, 100 µl aliquot were taken for Zr concentration measurement on the multicollector inductively coupled plasma mass spectrometer (MC-ICP-MS) and to verify complete Mo removal. Samples were then diluted to a final Zr concentration of 60 ng/g in 0.59 M HNO_3 + 0.28 M HF for MC-ICP-MS measurements.

Mass Spectrometry

Zr isotopic measurements were performed with a Thermo Scientific Neptune Plus using an Aridus 3 desolvating nebulizer at the Isotoparium, California Institute of Technology, following the methods of Tompkins *et al*. (2020). Measurements were performed in low mass resolution, using a static configuration monitoring masses 90 through 98. All Faraday cups were assigned 10^{11} Ω feedback resistors except for H1 (^{95}Mo) and H4 (^{98}Mo), which were assigned 10^{12} Ω feedback resistors to improve accuracy of Mo isobaric interference monitoring and corrections. Cup gains were calibrated daily.

Each unknown measurement was bracketed by measurements of the NIST RM8299 Zr iRM, a new Zr isotopic reference material prepared in a collaboration between the Isotoparium, the Arizona Heavy Isotopes Laboratory, and the U.S. National Institute of Standards and Technology (NIST) (Tissot *et al*., 2022). Bracketing standards were spiked at the same level as the samples. On-peak-zeros (OPZ) were measured before all samples and standards using a 50 s uptake and 20 s on-peak measurement of clean acid solution from the same batch used to dilute the samples, to monitor memory effects of the sample introduction system and remove background from all measurements. Sample and bracketing standard measurements consisted of 50 s of sample uptake, followed by 50 cycles of 4.192 s integration time each, for a total 210 s of static on-peak sample measurement. The Aridus 3 was rinsed for 360 s between samples using 0.59 M HNO3 + 0.56 M HF, before repeating the cycle for the next standard/unknown.

Within each sequence, two types of secondary reference materials were measured to monitor mass spectrometer performance and ensure data accuracy: 1) an industrial, pure Zr solution obtained from SPEX and calibrated by Tompkins *et al*. (2020); and 2) bulk-rock geostandard materials subjected to the same chemical processing as the samples studied here. The purpose of this approach is two-fold: 1) the SPEX solution allows monitoring the performance of the sample introduction system and mass spectrometer only, without any potentially complicating factors introduced by the ion exchange chemistry; and 2) results from geostandards allow monitoring the entire process, from sample dissolution, through chemistry and mass spectrometry, therefore demonstrating accuracy for our complete procedure.

The results of all reference materials measured during this study are shown in Figure S-2, where they are compared to their respective reference values. The excellent agreement between the measured $\delta^{94/90}Zr_{NIST}$ of these reference materials relative to published values demonstrates the accuracy of our results and ensures compatibility of our zircon-melt fractionation calculations relative to the existing Zr isotope literature.

Zirconium concentration measurements of glass by secondary ion mass spectrometry (SIMS)

Small fragments of each experiment were mounted in epoxy for trace element measurements of glass using secondary ion mass spectrometry (SIMS). SIMS analyses were performed using the CAMECA 1280HR SIMS instrument housed in the Swiss SIMS laboratory within the Center for Advanced Surface Analysis (CASA) at the University of Lausanne. Mounts were coated with ~35 nm of Au, deposited by Au evaporation or sputter coating under vacuum, prior to analysis. Analyses included positive secondary ions of ^{28}Si, ^{30}Si, ^{85}Rb, ^{90}Zr and ^{180}Hf. Samples were sputtered with an $^{16}O^{2-}$ primary ion beam (PIB) generated using a Hyperion-II RF plasma source, which was accelerated at 13 kV and focused to a ~4 µm spot. Secondary ions were accelerated at 10 kV. Analyses consisted of 90 s of pre-sputtering followed by 15 cycles with integration times of 2, 2, 8, 8 and 6 s, respective to the list of measured secondary ions above. Between pre-sputtering and measurement, the secondary ion beam was automatically centered within the transfer and field apertures; likewise, the secondary high voltage was automatically adjusted to compensate for sample charging if necessary. Analyses were standardized using NIST 610 and zircon 91500, both of which were measured once between every 4 unknown spots. Data processing was performed using a customized MATLAB reduction code using standard-sample-bracketing relative to the known Si and Zr concentrations of NIST 610 and zircon 91500, and the Rb concentration of NIST 610.

Constraining fractional Zr removal from the liquid (*f*)

The value of *f*, *i.e.*, the fraction of Zr removed from the liquid during each experimental run, was constrained using two independent approaches: i) using the *in-situ* determinations of Zr concentration in the glass from SIMS measurements; and ii) using Zr/Rb measurements from solutions produced after acid leaching during preparation for isotopic analyses. These two approaches and the mass-balance equations used are as follows:

Approach 1 – using *in-situ* glass [Zr] determinations

Given that the starting Zr concentration of each experiment (hereafter $[Zr]_{bulk}$) is known from the masses of the high-purity oxides used to make the starting base mixes (from Wang and Trail, 2019), we can use the concentration of Zr in the glass (hereafter $[Zr]_{glass}$) to determine the fraction of Zr removed from the liquid, *f*, using the following relation:

$$f = 1 - \frac{[Zr]_{glass}}{[Zr]_{bulk}} \qquad \text{Eq. S-1}$$

$[Zr]_{glass}$ values were determined *in-situ* using multiple SIMS spot analyses place in two randomly selected glass fragments set aside from each experimental run, prior to grinding and dissolution. The advantage of this approach is that, in addition to allowing quantification of a mean *f* for each experimental run product, it also allows evaluation of the spatial heterogeneity of $[Zr]_{glass}$. We use this spatial variability in $[Zr]_{glass}$ to assign an uncertainty to *f* that was then propagated through all subsequent calculations described below. Mean values of $[Zr]_{glass}$, calculated *f* values, and uncertainties assigned to both of these parameters, are reported in Table S3. These were calculated as the mean and standard deviation of all SIMS $[Zr]_{glass}$ determinations made in glass from each experiment.

Approach 2 – verifying *f* using bulk Zr/Rb measurements in solutions after acid leaching of glass

In order to verify the mean *f* values determined from Approach 1 above, a mass balance approach using the bulk Zr/Rb elemental ratios measured on aliquots of the experiments after dissolution was also performed. All fractions of glass, zircon, as well as the starting bulk base mixes analyzed for $\delta^{94/90}Zr$, were measured via Q-

ICPMS for Zr concentrations and Zr/Rb ratios to verify effective zircon-glass separation and to ensure accurate spiking. In the equations below, X_{glass} is taken to represent the mass fraction of liquid remaining in each experiment at quenching, X_{zircon} is the mass fraction of zircon formed in each experiment, and $f_{Zr/Rb}$ is the effective magnitude of f for the bulk glass constrained using this second approach. This second method using bulk solution measurements for constraining f provides a good consistency check of the *in-situ* method (Approach 1), but has the drawback that it erases (homogenizes) any spatial variability of $[Zr]_{glass}$ present within the glass, and therefore does not allow propagation of f variability through the isotope fractionation calculations described below. As such, we report values of $f_{Zr/Rb}$ in Table S3 as a consistency check, but the values of f and its standard deviation constrained using Approach 1 are preferred for all subsequent calculations and uncertainty propagations.

We can write mass balance equations for Rb and Zr in each experiment as:

$$[Rb]_{bulk} = [Rb]_{glass} \cdot X_{glass} + [Rb]_{zircon} \cdot (1 - X_{glass}) \quad \text{Eq. S-2}$$

and,

$$[Zr]_{bulk} = [Zr]_{glass} \cdot X_{glass} + [Zr]_{zircon} \cdot (1 - X_{glass}) \quad \text{Eq. S-3}$$

Dividing Eq. S-2 by Eq. S-3 yields

$$\left(\frac{Rb}{Zr}\right)_{bulk} = \frac{[Rb]_{glass} \cdot X_{glass} + [Rb]_{zircon} \cdot (1 - X_{glass})}{[Zr]_{glass} \cdot X_{glass} + [Zr]_{zircon} \cdot (1 - X_{glass})} \quad \text{Eq. S-4}$$

which upon re-arranging can be written as

$$\left(\frac{Zr}{Rb}\right)_{bulk} = \frac{[Zr]_{glass}}{[Rb]_{glass}} + \frac{[Zr]_{zircon}}{[Rb]_{glass}} \left(\frac{1}{X_{glass}} - 1\right) \quad \text{Eq. S-5}$$

Given the strong incompatibility of Rb in the zircon structure (Thomas *et al*., 2002), it is safe to assume that $[Rb]_{zircon}=0$, and one can re-write Eq. S-2 as

$$\frac{[Rb]_{bulk}}{X_{glass}} = [Rb]_{glass} \quad \text{Eq. S-6}$$

By substituting Eq. S-6 into Eq. S-5 and re-arranging terms, one can solve for X_{glass} as

$$X_{glass} = 1 - \frac{\left(\frac{Zr}{Rb}\right)_{bulk} - \left(\frac{Zr}{Rb}\right)_{glass}}{\frac{[Zr]_{zircon}}{[Rb]_{bulk}}} \quad \text{Eq. S-7}$$

The fraction of zircon (X_{zircon}) formed in each experiment can be calculated as:

$$X_{zircon} = 1 - X_{glass} \quad \text{Eq. S-8}$$

And given that the fraction of Zr removed from the liquid in the form of zircon can be expressed as:

$$f_{ZrRb} = \frac{[Zr]_{zircon} \cdot X_{zircon}}{[Zr]_{bulk\ initial}} \quad \text{Eq. S-9}$$

Equations S-7, S-8, and S-9 can be combined into a final expression for determining a mean f_{RbZr} for each experiment, as follows:

$$f_{ZrRb} = \frac{[Zr]_{zircon} \cdot \left(1 - \left(1 - \frac{\left(\frac{Zr}{Rb}\right)_{bulk} - \left(\frac{Zr}{Rb}\right)_{glass}}{\frac{[Zr]_{zircon}}{[Rb]_{bulk}}}\right)\right)}{[Zr]_{bulk\ initial}} \qquad \text{Eq. S-10}$$

For these calculations, zirconium in zircon was assumed to be stoichiometric (*i.e.*, $[Zr]_{zircon}$ = 49.77 wt. %), and $[Zr]_{bulk}$ and $[Rb]_{bulk}$ were calculated using the known concentrations of the starting oxides and their masses in the base mixtures as reported by Wang and Trail (2019). The values for $(Zr/Rb)_{glass}$ used for f_{RbZr} calculations are those determined directly from our experiment dissolutions, measured by Q-ICPMS. The calculated values of f_{RbZr} determined this way are reported in Table S3, where they are compared with the values of f determined using our first calculation approach described above. The calculated values of f_{RbZr} are in excellent agreement with the mean f values estimated for $[Zr]_{glass}$ via SIMS, thus lending further confidence of our calculations of Zr fractional removal.

As mentioned above, the mean and standard deviation of f determined using SIMS measurements in glass are the preferred values of f used for all α calculations for two main reasons: i) the in-situ approach allows us to evaluate the spatial variability of Zr removal within each experiment, and thus assign an uncertainty to f for uncertainty propagations; and ii) the variability in the glass allows us to evaluate how far (or close) each experiment was from equilibrium at the time of quenching, which is a qualitative indicator of the magnitude of the Zr concentration gradients within the liquid at time of quenching . The distribution of $[Zr]_{glass}$ values, calculated from n= 20–90 spot determinations of Zr concentration in experimental glasses via SIMS, are shown in Figure S-5. Distributions of Zr concentrations are shown as kernel density estimates (KDE) using a Gaussian smoothing kernel and optimal bandwidths for each distribution calculated using the methods of Botev *et al*. (2010). Graphs were plotted using the *DensityDist* Matlab code of Pullen *et al*. (2014). It is clear from Figure S-5 that glasses from high-T (low-f) experiments exhibit a much larger spatial variability in $[Zr]_{glass}$, and that this variability in $[Zr]_{glass}$ decreases with increasing mean f, reflecting the progressive obliteration of diffusive boundary layers in the liquid as Zr removal from the liquid increases.

Zr Isotope Data Processing and Modelling Approach

Verification of Zr mass-balance for experimental run products

An important first step to data interpretation is to verify that zirconium concentration and isotopic composition of measured glass and bulk zircon pairs conform to mass-balance with respect to known starting bulk compositions. For each experimental glass-zircon pair, the fraction of Zr removed from the liquid (f) as well as the isotopic composition (expressed as $\delta^{94/90}$Zr) for the two phases and their associated uncertainties was determined (Tables S2 and S3). Using mass-balance, the *reconstructed* bulk isotopic composition of a two-component mixture (R_{mix}) between the measured glass (R_{glass}) and zircon (R_{zircon}) can be calculated as:

$$\left(\frac{^{94}Zr}{^{90}Zr}\right)_{mix} = \left(\frac{^{94}Zr}{^{90}Zr}\right)_{glass} \cdot \left(\frac{^{90}Zr_{glass}}{^{90}Zr_{mix}}\right) \cdot (1 - f) + \left(\frac{^{94}Zr}{^{90}Zr}\right)_{zircon} \cdot \left(\frac{^{90}Zr_{zircon}}{^{90}Zr_{mix}}\right) \cdot f \qquad \text{Eq. S-11}$$

Expressing the $^{94/90}$Zr values in Eq. S-11 using delta notation, and because the concentrations of isotope ^{90}Zr (*i.e.*, the most abundant isotope of Zr) are very close to equal in the zircon and in the glass (*i.e.*, $[^{90}Zr]_{glass} \approx [^{90}Zr]_{zircon} \approx [^{90}Zr]_{mix}$), this expression can be reduced to

$$\delta^{94/90}Zr_{mix} = \delta^{94/90}Zr_{glass} \cdot (1 - f) + \delta^{94/90}Zr_{zircon} \cdot f \qquad \text{Eq. S-12}$$

Using the calculated *f* values for each experiment (Table S2), and their respective $\delta^{94/90}$Zr for each glass-zircon pair (Table S3), a reconstructed $\delta^{94/90}$Zr value for the mix is calculated and compared with the starting $\delta^{94/90}$Zr of the experiments (*i.e.*, $\delta^{94/90}$Zr of base mixes) to assess mass balance. Calculation of Eq. S-12 was conducted using a Monte Carlo approach with 10^5 realizations and assuming normal distributions for all parameters, to obtain a value of the mix that considers all uncertainties. The result of these calculations is shown in Figure 1b of the main text, where it is compared to the mean $\delta^{94/90}$Zr of all base mixes (gray horizontal band). From these calculations it can be seen that all experiments except ZrGT13 conform to mass-balance with respect to the starting bulk $\delta^{94/90}$Zr composition within uncertainties, therefore reinforcing the notion that we can use the $\delta^{94/90}$Zr values determined from these three components (bulk, glass and zircon) to approximate $\alpha_{\text{zircon-melt}}$ as follows below. Two reasons that can explain the small offset of ZrGT13 from perfect mass balance can be: i) the distribution of $[\text{Zr}]_{\text{glass}}$ determined via SIMS spot analyses from glass fragments that were not digested may be an imperfect descriptor of the true variability of *f* (*i.e.*, internal compositional gradients) present in the liquid at the time of quenching to a glass; and/or ii) because the entire run product was not analyzed (*i.e.*, experimental capsules were first sliced in half longitudinally and only ~one half of the load mass, minus fragments set aside for SIMS, were analyzed for $\delta^{94/90}$Zr), the strong compositional gradients present within the glass mean that small deviations from ideal mass-balance can be expected. Nevertheless, as pointed out above, only one experiment deviates from mass-balance expectations, and this experiment is therefore not given weight towards our final interpretations.

Quantifying the isotopic fractionation coefficient, $\alpha_{\text{zircon-melt}}$

Due to the slow diffusivity of tetravalent ions in zircon (Cherniak *et al*., 1997), the growth of zircon from a magma (natural or experimental) removes Zr as a Rayleigh-type process even if chemical and isotopic equilibrium partitioning between the solid and melt are maintained (Ibañez-Mejia and Tissot, 2019). In an equilibrium Rayleigh-type system, the isotopic compositions of the evolving liquid, instantaneous solid, and bulk solid can be expressed using the following equations (Criss, 1999):

$$R_{liq} = R_0 f^{\alpha-1} \qquad \text{Eq. S-13}$$

$$R_{inst\ solid} = R_0 \alpha f^{\alpha-1} \qquad \text{Eq. S-14}$$

$$R_{bulk\ solid} = \frac{R_0 - R_{liq} \cdot f}{(1-f)} \qquad \text{Eq. S-15}$$

where R_0 is the initial isotopic composition of the bulk system, R_{liq} is the isotopic composition of the liquid, $R_{inst\ solid}$ and $R_{bulk\ solid}$ are the isotopic compositions of the instantaneous and bulk solids removed from the liquid, respectively, α is the equilibrium fractionation coefficient between solid and liquid, and *f* is the fraction of Zr removed from the liquid in the form of solid. No fractionation occurs when $\alpha_{\text{zircon-melt}} = 1$. Larger fractionations result in a greater magnitude of divergence from 1. A graphical representation of the evolution of a Rayleigh-type system is shown in Figure S-3a, where the curves represented by Eqs. S-13 through S-15 are highlighted for greater clarity.

The Zr isotopic fractionation coefficient between zircon and melt $\alpha_{\text{zircon-melt}}$, is defined as follows:

$$\alpha_{zircon-melt} = \frac{R_{inst\ solid}}{R_{liq}} \qquad \text{Eq. S-16}$$

Eq. S-16 implies that one could directly determine $\alpha_{\text{zircon-melt}}$ if one could measure the isotopic composition of a liquid and instantaneous solid pair in direct equilibrium. However, as zircon crystals progressively grow from a liquid, they integrate multiple layers with variable $R_{inst\ solid}$ (Eq. S-14) as their surrounding melt evolves following Eq. S-13 to produce a zoned, growth-integrated $R_{bulk\ solid}$ (Eq. S-15). Given our experimental

approach as described in the Methods section above, $R_{inst\ solid}$ is an unmeasurable value, and our experiments can only recover $R_{bulk\ solid}$ for each run. Therefore, since we cannot calculate $\alpha_{zircon\text{-}melt}$ directly, we calculate it by inversion of this Rayleigh-type system. Below we identify four distinct solutions to approximate $\alpha_{zircon\text{-}melt}$ using our measurements:

Solution 1 – apparent α, or α_{app}:

The simplest yet arguably least accurate way of approximating α from our experiments would be to calculate an apparent value (dubbed 'α_{app}') directly from the measured $R_{bulk\ solid}$ and R_{liq} values, as follows:

$$\alpha_{app} = \frac{R_{bulk\ solid}}{R_{liq}} \qquad \text{Eq. S-17}$$

In contrast to $R_{inst\ solid}$, $R_{bulk\ solid}$ is a measured quantity from our experiments. However, because $R_{bulk\ solid}$ represents only the mean composition of a growth-zoned zircon, α_{app} does not accurately reflect the magnitude of $\alpha_{zircon\text{-}melt}$, but rather provides a maximum permissible value of the latter. This is illustrated in Figure S-3b where, using a pre-imposed $\alpha_{zircon\text{-}melt}$=0.99997 (see Fig. S-3a), the values of $\alpha_{zircon\text{-}melt}$ and α_{app} were calculated using Eqs. S-16 and S-17, respectively, as a function of *f*. It can be concluded from Figure S-3b that: i) the magnitude of α_{app} always overestimates the magnitude of the 'true' $\alpha_{zircon\text{-}melt}$; ii) α_{app} approaches $\alpha_{zircon\text{-}melt}$ as *f* tends to 0; and iii) the magnitude of the offset between α_{true} and α_{app} is not significantly amplified (*i.e.*, α_{app} become larger than α_{true} by more than ~50%) for *f* values below 0.5. This means that α_{app}, which can be easily calculated for each of our experiments, in all cases provides a maximum constraint on the magnitude of the true $\alpha_{zircon\text{-}melt}$ governing the experiment.

Solution 2 – constraining α using R_0 and R_{liq}, or α_{liq}:

By rearranging Eq. S-13 to solve for α, one can obtain an expression that uses the measured compositions of the bulk system (R_0) and the residual liquid (R_{liq}) at a given *f* value to obtain a solution for $\alpha_{zircon\text{-}melt}$, which we call α_{liq}.

$$\alpha_{liq} = \frac{log(\frac{R_{liq}}{R_0})}{log(f)} + 1 \qquad \text{Eq. S-18}$$

This analytical solution only considers the isotopic compositions of the bulk system (R_0) and liquid (R_{liq}), but ignores that of the cumulative zircon ($R_{bulk\ solid}$).

Solution 3 – constraining α using R_0 and $R_{bulk\ solid}$, or α_{solid}:

By rearranging Eq. S-15 and substituting Eq. S-13 to solve for α, one obtains an expression that uses the measured compositions of the bulk system (R_0) and the cumulative zircon ($R_{bulk\ solid}$) at a given *f* value to solve for the effective $\alpha_{zircon\text{-}melt}$, which we call α_{solid}.

$$\alpha_{solid} = \frac{log(1-\frac{(1-f)R_{bulk\ solid}}{R_0})}{log(f)} \qquad \text{Eq. S-19}$$

In contrast to Solution 2, this analytical solution considers only the isotopic composition of the bulk system (R_0) and the cumulative zircon ($R_{bulk\ solid}$) but ignores that of the liquid (R_{liq}).

Solution 4 – constraining α using R_{liq}, and $R_{bulk\ solid}$, or $\alpha_{glass\text{-}zircon}$:

Since Solution 2 (α_{liq}) and Solution 3 (α_{solid}) above do not consider both of the phases produced by each experiment, they consistently ignore important constraints on $\alpha_{zircon\text{-}melt}$ imposed by our measured isotopic compositions. Therefore, we derive one last solution that uses both available constraints. In Solution 1 above,

we divided the composition of the measured cumulative solid ($R_{bulk\ solid}$) by the liquid (R_{liq}) to obtain α_{app} (Eq. S-17). We can take this equation a step further by equating $R_{bulk\ solid}$ and R_{liq} to their analytical solutions, Eqs. S-15 and S-13, respectively.

$$\frac{R_{bulk\ solid}}{R_{liq}} = \frac{\frac{R_0 - (R_0 f^{\alpha-1})\cdot f}{(1-f)}}{R_0 f^{\alpha-1}} \quad \text{Eq. S-20}$$

Solving for α, one finds an expression that combines the measured compositions of the cumulative solid ($R_{bulk\ solid}$), the liquid (R_{liq}), and *f*, as follows:

$$\alpha_{glass-zircon} = \frac{ln\left(\frac{1}{f+\frac{R_{bulk\ solid}(1-f)}{R_{liq}}}\right)}{ln(f)} + 1 \quad \text{Eq. S-21}$$

Because this solution for α considers most of the constraints our measurements impose on each experimental product, *i.e.*, $R_{bulk\ solid}$, R_{liq}, and *f*, we favor the results obtained using this last solution whenever possible.

In this study, we test the four aforementioned approaches for constraining $\alpha_{zircon\text{-}melt}$, namely: α_{app}, α_{liq}, α_{solid}, and $\alpha_{glass\text{-}zircon}$. In practice, we inverted Eqs. S-17, S-18, S-19 and S-20 using a Monte Carlo approach with 10^4 realizations, taking into consideration the uncertainties of all input parameters to output a mean α for each method with a total propagated uncertainty. Uncertainties for each parameter were assumed to be normally distributed. For a system in perfect equilibrium, solutions 2, 3 and 4 should return equivalent values of α. However, our modelling results summarized in Table S3 show that the samples are not in perfect equilibrium, as these different solutions do not always yield concordant α values. Of all solutions, α_{liq} and α_{solid} consistently return modelled results that do not match the measured isotopic composition of the parameter left unconstrained by the calculations. α_{solid} behaves as the worst solution, as it consistently violates the constraint that α_{app} must be the maximum permissible α. In contrast, α_{liq} tends to underestimate the magnitude of fractionation because it does not consider the isotopic composition of the strongly fractionated solids. On the other hand, the solutions that we consider better reflect the isotopic results are α_{app} or $\alpha_{glass\text{-}zircon}$. For samples with low *f* values (<0.5), the $\alpha_{glass\text{-}zircon}$ solution does not do an adequate job of capturing the unexpectedly low $\delta^{94/90}$Zr measured for the cumulative zircon which, as described in the main text and below, we argue has an isotopic composition dominated by kinetic isotope fractionation. Thus, for run products with f <0.5, α_{app} was selected as the preferred solution, as it provides a *maximum* constraint on the magnitude of equilibrium isotope fractionation. We further note that, in the case of zircon crystallization, kinetic isotope fractionation during diffusion-limited growth implies that light Zr isotopes will be delivered more efficiently to a growing zircon seed than heavier isotopes, thereby making the cumulative solid lower in $\delta^{94/90}$Zr than expected from vibrational equilibrium alone (Watson and Müller, 2009; Meheut *et al*., 2021) and amplifying the magnitude of α_{app}. Thus, even though our low-*f* experiments significantly depart from an equilibrium Rayleigh behavior due to kinetic isotope fractionation, both equilibrium and kinetic effects work in the same direction (*i.e.*, both make a zircon's $\delta^{94/90}$Zr 'light'), and so α_{app} from our experiments consistently provides a maximum permissible value for the magnitude of the $\alpha_{zircon\text{-}melt}$ at equilibrium.

Figure S-4 shows the maximum constraints on the magnitude of isotopic fractionation for each experiment as imposed by Eq. S-17 (α_{app}), compared to the *ab initio* models of Chen *et al*. (2020) and Meheut *et al*. (2021).

In experiments with f <0.5, kinetic isotope effects are dominant (see main text and next section for discussion), and so the magnitude of α_{app} determined from these experimental products was preferred and considered as a maximum permissible value of $\alpha_{zircon\text{-}melt}$. For experiments with larger f values (>0.5), Solution 4, which takes into consideration all measured constraints for each experiment, was preferred. Accordingly, a preferred value for α was selected for each experiment and this value is presented in Table S4. These values are the ones used for all figures and discussions throughout the main text.

Numeric model for kinetic isotope fractionation during zircon growth

Bindeman and Melnik (2022) recently presented a numerical solution to the problem of kinetic Zr isotope fractionation during diffusion-limited zircon growth under variable conditions. To illustrate how kinetic isotope effects may affect the results of our experiments, we performed numerical calculations using a slightly adjusted version of the freely available code of Bindeman and Melnik (2022). The parameters used were as follows: 1) the velocity of the outermost boundary (*i.e.*, the 'plagioclase front' of Bindeman and Melnik (2022)) was set to zero, to account for the fact that no phases other than zircon were formed during our experiments and the outer capsule boundary remained in a static position; 2) the M-factor was set to 1.51, which is the middle of the range of our experiments and in agreement with base mixture GT02 used here (see Table S1); 3) because our higher T experiments were conducted at 1400 ˚C and this is the temperature at which experimental zircon nucleated (Wang and Trail, 2019), the bulk Zr concentration of the model was set to the concentration that would saturate zircon at this temperature given the prescribed M-factor and using the parameters of Boehnke *et al.* (2013), as used in the Bindeman and Melnik (2022) code. Because the zircon fractions analyzed here represent bulk cumulative zircon rather than instantaneous compositions, and the code of Bindeman and Melnik (2022) only outputs instantaneous solid compositions as a function of crystal radius, a simple addition was made to their code to compute the cumulative $\delta^{94/90}$Zr of zircon as a function of crystal radius by integrating the instantaneous zircon composition over a spherical geometry. The calculation performed here considered a temperature decrease of 50 K over the course of 120 hours, which was a typical experimental time for the runs of Wang and Trail (2019). Water contents were set to 10 wt. % as in the experiments of Wang and Trail (2019).

The results of the numerical simulation described above are shown graphically in Figure 2 in the main text and in Figure S-6. The curve in Figure 2 highlights the slope of the $1000\ln(\alpha_{zircon\text{-}melt})$ *vs.* $10^6/T$ relation that would result from a kinetic control on Zr isotope fractionation. In addition to the slope of this line reproducing well our results from the high-temperature (1300 – 1400 ˚C) experiments, this modeled line also crucially: i) *does not* intersect the origin of this graph as would be required by equilibrium isotope fractionation (*e.g.*, Young *et al*., 2015); ii) *does not* resemble the slopes of the equilibrium fractionation models of Chen *et al*. (2020) and Méheut *et al*. (2021); and iii) has a slope that is much closer to the model proposed by Guo *et al*. (2020), which was derived by linearly fitting apparent $\Delta^{94/90}$Zr values obtained from Rayleigh inversion of $\delta^{94/90}$Zr zoning in natural zircon crystals. Altogether, these observations indicate that the low-f experiments conducted at high temperature are strongly affected by non-equilibrium isotope fractionation. Figure S-6 shows other simulation outputs relevant to the run depicted in Figure 2 and/or that are useful scaling parameters to quantify the magnitude of non-equilibrium isotope fractionation (e.g., Watson and Müller, 2009), namely (a) the calculated zircon radius *vs.* time, (b) zircon-melt Zr partition coefficient *vs.* time, (c) diffusivity (D) of Zr in the melt *vs.* time; d) calculated rate of zircon growth (*i.e.*, radial velocity of phase boundary migration, R) *vs.* crystal radius; e) R/D scaling parameter *vs.* crystal radius; and (f) resulting zircon $\delta^{94/90}$Zr *vs.* crystal radius relationship with curves for both instantaneous as well as cumulative zircon $\delta^{94/90}$Zr values.

Supplementary Tables

Table S-1 Experimental and compositional parameters of zircon growth experiments. Temperature (T), time (t), pressure (P).

Experiment	ZrGT51	ZrGT28	ZrGT26	ZrGT27	ZrGT33	ZrGT19	ZrGT17	ZrGT16	ZrGT13	ZrGT46	ZrGT01	ZrGT45	ZrGT02	ZrGT03
Base (Melt)	GT03	GT02	GT02	GT01	GT08	GT01	GT03	GT02	GT01	GT02	GT01	GT01	GT02	GT03
T (°C)	1300	1400	1300	1400	1400	1300	1150	1150	1150	1100	925	1100	925	925
t (hr)	120	120	120	120	120	120	312	312	312	288	120	288	120	120
P (GPa)	1.0	1.0	1.0	1.0	1.0	1.0	1.0	1.0	1.0	1.0	1.0	1.0	1.0	1.0
ASI melt	0.93	1.09	1.08	1.31	0.91	1.31	0.9	1.15	1.25	1.16	0.95	1.32	1.18	1.33
ASI melt, 1 s.d.	0.01	0.02	0.03	0.02	0.01	0.03	0.03	0.03	0.04	0.03	–	0.04	–	–
A/NK	1.42	1.7	1.64	2.04	1.37	2.04	1.41	1.84	1.95	1.76	1.52	2.02	1.97	2.24
A/NK, 1 s.d.	0.02	0.04	0.02	0.02	0.02	0.05	0.03	0.05	0.07	0.05	–	0.08	–	–
M	1.76	1.51	1.51	1.21	1.72	1.18	1.75	1.35	1.23	1.43	1.70	1.23	1.35	1.17
M 1, s.d.	0.03	0.03	0.05	0.02	0.02	0.02	0.07	0.03	0.04	0.06	–	0.04	–	–
Melt type	ML	PL	PL	PL	ML	PL	ML	PL	PL	PL	ML	PL	PL	PL
ZrO_2 (wt. %)	2.87	2.52	2.52	2.24	3.85	2.24	2.87	2.52	2.24	2.52	2.24	2.24	2.52	2.87
Zr (ppm)	21247	18656	18656	16583	28502	16583	21247	18656	16583	18656	16583	16583	18656	21247
$T_{saturation}$ (°C)	1560	1614	1614	1699	1680	1713	1563	1682	1690	1648	1501	1690	1681	1820
$\ln(D_{Zr})$	3.15	3.28	3.28	3.40	2.86	3.40	3.15	3.28	3.40	3.28	3.40	3.40	3.28	3.15
D_{Zr}	23.4	26.7	26.7	30.0	17.5	30.0	23.4	26.7	30.0	26.7	30.0	30.0	26.7	23.4

Table S-2 Calculated values of Zr fractional removal (*f*) from the liquid from mass-balance, ranked by increasing *f*

Experiment Base (Melt)	ZrGT51 GT03	ZrGT28 GT02	ZrGT26 GT02	ZrGT27 GT01	ZrGT33 GT08	ZrGT19 GT01	ZrGT17 GT03	ZrGT16 GT02	ZrGT13 GT01	ZrGT46 GT02	ZrGT01 GT01	ZrGT45 GT01	ZrGT02 GT03	ZrGT03 GT02
Zr concentrations in glass measured by SIMS and resulting *f* values (means and standard deviations)														
$[Zr]_{glass}$ (µg/g)	18760	16074	15528	13621	21290	7827	5088	3050	2370	1873	1699	1534	794	601
s.d.	592	869	362	727	494	2710	551	196	151	89	60	48	35	58
$f_{Zr\text{-}glass}$	0.12	0.14	0.17	0.18	0.25	0.53	0.76	0.84	0.86	0.90	0.90	0.91	0.963	0.97
s.d.	0.06	0.09	0.04	0.09	0.03	0.33	0.05	0.02	0.02	0.01	0.01	0.01	0.003	0.01
Zr/Rb concentration ratios in bulk-glass aliquots produced from acid leaching, and resulting mean *f* calculations														
$(Zr/Rb)_{bulk}$	42.49	37.31	37.31	33.17	57.00	33.17	42.49	37.31	33.17	37.31	33.17	33.17	42.49	37.31
$(Zr/Rb)_{glass}$	35.40	31.03	30.01	26.05	42.45	15.15	8.61	4.71	3.85	3.58	2.73	2.66	1.39	2.57
$[Rb]_{bulk}$ (µg/g)	500	500	500	500	500	500	500	500	500	500	500	500	500	500
$[Zr]_{bulk}$ (µg/g)	21247	18656	18656	16583	28502	16583	21247	18656	16583	18656	16583	16583	21247	18656
$[Zr]_{zircon}$ (µg/g)	497661	497661	497661	497661	497661	497661	497661	497661	497661	497661	497661	497661	497661	497661
X_{glass}	0.9929	0.9937	0.9927	0.9929	0.9854	0.9819	0.9660	0.9672	0.9705	0.9661	0.9694	0.9693	0.9587	0.9651
X_{zircon}	0.0071	0.0063	0.0073	0.0071	0.0146	0.0181	0.0340	0.0328	0.0295	0.0339	0.0306	0.0307	0.0413	0.0349
$f_{Zr/Rb}$	0.17	0.17	0.20	0.21	0.26	0.54	0.80	0.87	0.88	0.90	0.92	0.92	0.97	0.93
	High-T, Low-*f*						**Low-T, High-*f***							

Table S-3 Zr isotope results for all base mix, glass, and zircon fractions analyzed.

Experiment	ZrGT51	ZrGT28	ZrGT26	ZrGT27	ZrGT33	ZrGT19	ZrGT17	ZrGT16	ZrGT13	ZrGT46	ZrGT01	ZrGT45	ZrGT02	ZrGT03
Base mix														
($\delta^{94/90}$Zr)	-0.057	-0.052	-0.052	-0.054	-0.059	-0.054	-0.057	-0.052	-0.054	-0.052	-0.054	-0.054	-0.052	-0.057
2SE	0.007	0.005	0.005	0.007	0.010	0.007	0.007	0.005	0.007	0.005	0.007	0.007	0.005	0.007
n	14	27	27	14	8	14	14	27	14	27	14	14	27	14
MSWD	0.67	1.06	1.06	0.90	0.78	0.90	0.67	1.06	0.90	1.06	0.90	0.90	1.06	0.67
Glass														
($\delta^{94/90}$Zr)	-0.055	-0.052	-0.057	-0.051	-0.050	-0.054	0.123	0.052	0.044	0.091	-0.004	0.060	0.062	0.054
2SE	0.013	0.016	0.016	0.013	0.013	0.013	0.013	0.013	0.011	0.013	0.013	0.013	0.013	0.013
n	5	4	4	6	6	5	5	5	6	5	5	5	6	5
MSWD	1.36	0.95	0.53	0.59	0.43	0.88	1.48	1.07	1.68	0.38	0.82	1.01	1.60	0.34
Zircon														
($\delta^{94/90}$Zr)	-0.158	-0.116	-0.168	-0.135	-0.068	-0.128	-0.138	-0.115	-0.115	-0.084	-0.094	-0.084	-0.074	-0.088
2SE	0.011	0.009	0.011	0.011	0.013	0.011	0.013	0.013	0.011	0.013	0.011	0.011	0.011	0.013
n	7	9	6	6	6	6	5	5	6	5	6	6	6	5
MSWD	1.48	0.27	0.55	0.29	0.56	0.83	1.64	0.62	1.29	0.28	1.50	0.74	0.06	0.49

Table S-4 Calculated values of f and $\Delta^{94/90}$Zr from Monte Carlo inversion of Zr isotope results, ranked by increasing f. Solutions 1 through 4, as described in the supplementary text, are expressed as 1000 x ln (α). Values in red have calculated 1000 x ln (α) magnitudes larger than 1000 x ln (α_{app}), and thus violate the constraint that 1000 x ln (α_{app}) provides a maximum permissible value for the 1000 x ln ($\alpha_{zircon\text{-}melt}$) of each experiment.

Experiment	ZrGT51	ZrGT28	ZrGT26	ZrGT27	ZrGT33	ZrGT19	ZrGT17	ZrGT16	ZrGT13	ZrGT46	ZrGT01	ZrGT45	ZrGT02	ZrGT03
Mass fraction of Zr removed from liquid														
$f_{Zr\text{-}glass}$	0.12	0.14	0.17	0.18	0.25	0.53	0.76	0.84	0.86	0.90	0.90	0.91	0.96	0.97
± s.d.	0.06	0.09	0.04	0.09	0.03	0.33	0.05	0.02	0.02	0.01	0.01	0.01	0.00	0.01
Solution 1 – α_{app} from Eq. S-17														
$\Delta^{94/90}Zr_{zircon\text{-}melt}$	-0.103	-0.064	-0.111	-0.084	-0.018	-0.074	-0.261	-0.167	-0.159	-0.175	-0.090	-0.144	-0.136	-0.142
± 2s	0.017	0.018	0.019	0.017	0.018	0.017	0.018	0.018	0.016	0.018	0.019	0.017	0.017	0.020
Solution 2 – α_{liq} from Eq. S-18														
$\Delta^{94/90}Zr_{zircon\text{-}melt}$	-0.016	-0.013	0.016	-0.015	-0.031	0.000	-0.126	-0.057	-0.050	-0.062	-0.022	-0.048	-0.035	-0.032
± 2s	1.463	18.841	3.027	7.467	0.088	0.630	0.083	0.018	0.015	0.012	0.007	0.008	0.006	0.009
Solution 3 – α_{solid} from Eq. S-19														
$\Delta^{94/90}Zr_{zircon\text{-}melt}$	-0.108	-0.067	-0.125	-0.090	-0.010	-0.110	-0.180	-0.178	-0.188	-0.125	-0.154	-0.124	-0.172	-0.271
± 2s	0.022	0.020	0.017	0.027	0.019	0.813	2.773	0.079	0.093	0.068	0.066	0.059	0.109	0.433
Solution 4 – $\alpha_{glass\text{-}zircon}$ from Eq. S-21														
$\Delta^{94/90}Zr_{zircon\text{-}melt}$	-0.097	-0.059	-0.101	-0.076	-0.016	-0.052	-0.139	-0.077	-0.070	-0.068	-0.035	-0.055	-0.040	-0.040
± 2s	0.020	0.021	0.019	0.022	0.016	0.062	0.054	0.016	0.014	0.011	0.008	0.008	0.006	0.010
	High-T, Low-*f*						**Low-T, High-*f***							

Table S-5 Summary of preferred *f*, α, and $\Delta^{94/90}Zr$ values from all experiments used for figures in the main text.

Experiment	ZrGT51	ZrGT28	ZrGT26	ZrGT27	ZrGT33	ZrGT19	ZrGT17	ZrGT16	ZrGT13	ZrGT46	ZrGT01	ZrGT45	ZrGT02	ZrGT03
mean f	0.12	0.14	0.17	0.18	0.25	0.53	0.76	0.84	0.86	0.90	0.90	0.91	0.96	0.97
Solution method	app	app	app	app	app	app	glass-zircon	glass-zircon	glass-zircon	glass-zircon	glass-zircon	glass-zircon	glass-zircon	glass-zircon
α	0.999897	0.999936	0.999889	0.999916	0.999982	0.999926	0.999861	0.999923	0.999930	0.999932	0.999965	0.999945	0.999960	0.999960
2s	0.000017	0.000018	0.000019	0.000017	0.000018	0.000017	0.000054	0.000016	0.000014	0.000011	0.000008	0.000008	0.000006	0.000010
$\Delta^{94/90}Zr_{zircon-melt}$	-0.103	-0.064	-0.111	-0.084	-0.018	-0.074	-0.139	-0.077	-0.070	-0.068	-0.035	-0.055	-0.040	-0.040
2s	0.017	0.018	0.019	0.017	0.018	0.017	0.054	0.016	0.014	0.011	0.008	0.008	0.006	0.010
	High-T, Low-*f*						**Low-T, High-*f***							

Supplementary Figures

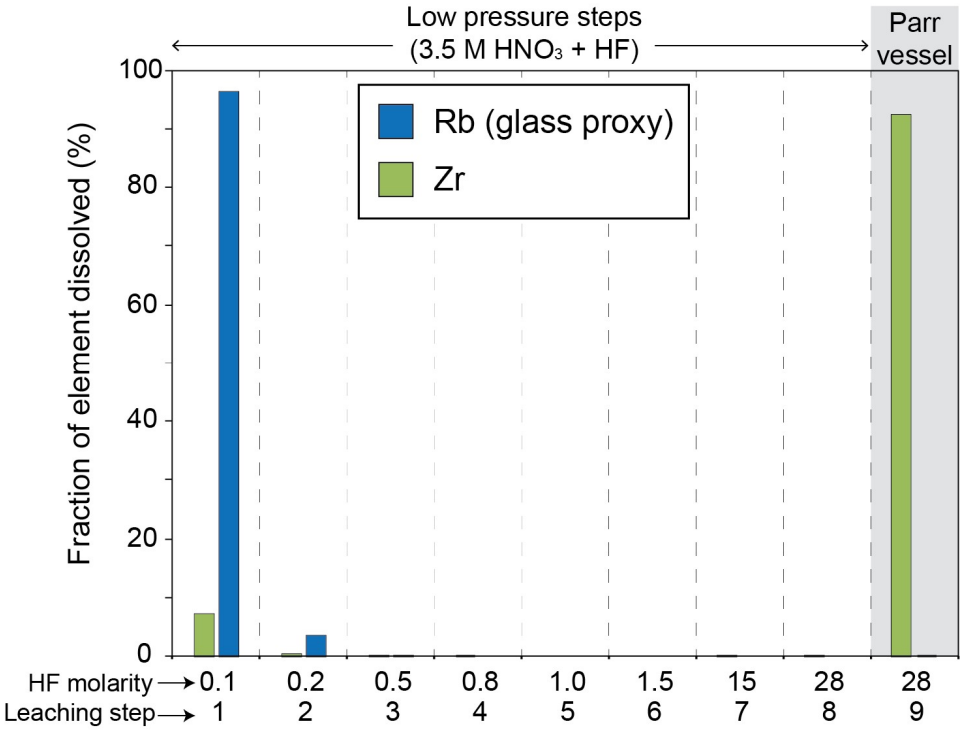

Figure S-1 Calibrated separation procedure using the fraction of total Rb and Zr measured in the supernatant from each step as a proxy for zircon-glass separation. Complete glass dissolution is achieved using 0.1 and 0.2 M HF steps at low pressure, while zircon is not reacted until using 28 M HF in a Parr® vessel.

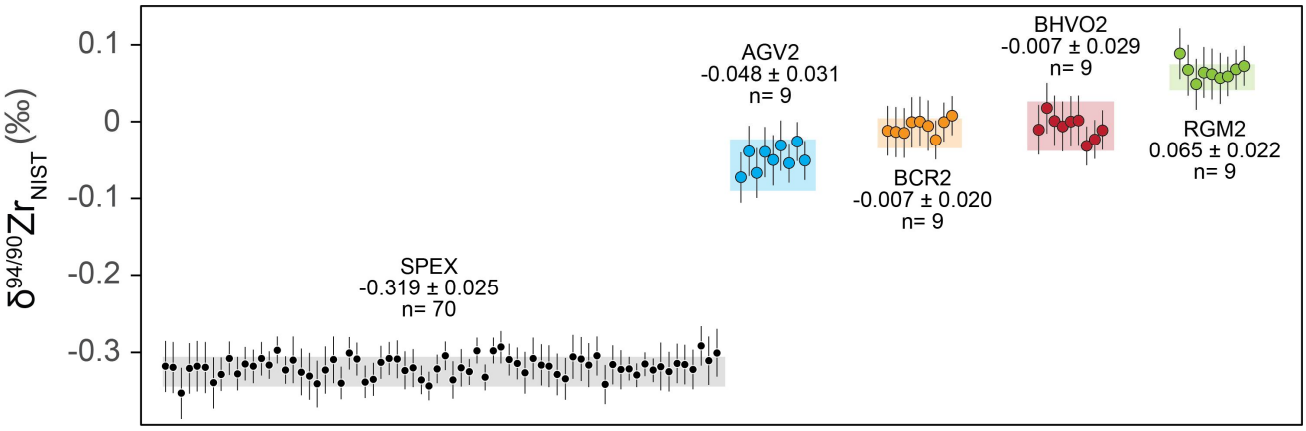

Figure S-2 Results of Zr reference materials measured during this study, reported as $\delta^{94/90}Zr_{NIST}$. The reported values are unweighted means and uncertainties are 2 standard deviations of the data. Shaded bars represent the reference values for each material considering results published in the literature and our long-term reproducibility, as follows: SPEX: -0.325 ± 0.019 ‰; AGV2: -0.057 ± 0.034 ‰; BCR2: -0.015 ± 0.019 ‰; BHVO2: -0.006 ± 0.032 ‰; RGM2: 0.058 ± 0.016 ‰.

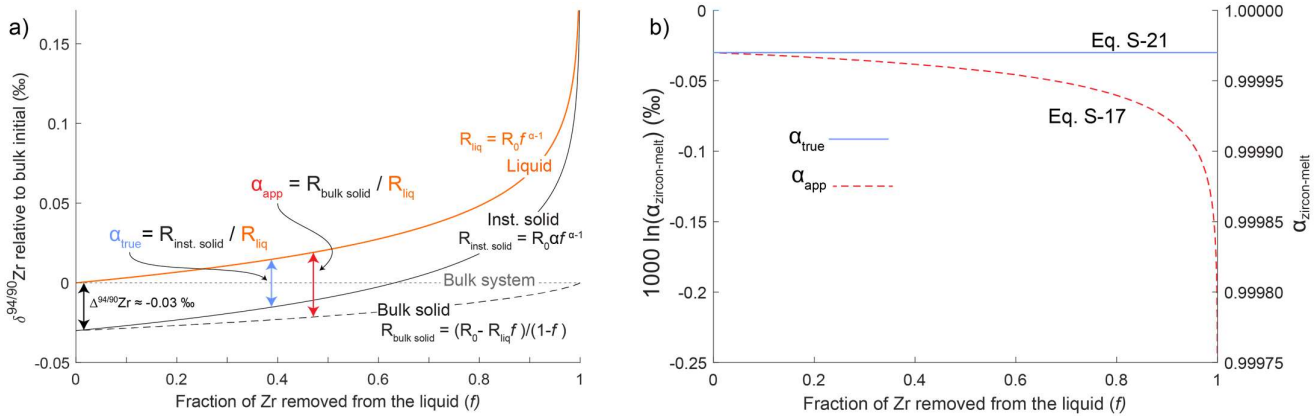

Figure S-3 a) Forward model showing the isotopic evolution of a Rayleigh system as a function of Zr removal from the liquid (*f*) where $1000\ln\alpha^{94/90}Zr_{mineral\text{-}zircon}$ (‰) ≈ 0.03, or α = 0.99997. The dotted grey line represents the initial bulk system, the solid black line represents the instantaneous solid, the dashed black line represents the bulk solid, and the orange line represents the liquid. Also shown are equations S-13 through S-17. **b)** Calculated values of $\alpha_{zircon\text{-}melt}$ (solid blue line), the true isotopic fractionation coefficient of the system according to Eq. S-4, and α_{app} (red dashed line), the apparent isotopic fractionation coefficient calculated from our experiments according to Eq. S-5, from the forward model of panel a. α_{app} approaches $\alpha_{zircon\text{-}melt}$ as *f* tends to 0 and increases with increasing *f*, meaning that α_{app} always provides a maximum constraint on the magnitude of $\alpha_{zircon\text{-}melt}$. Note that the divergence between $\alpha_{zircon\text{-}melt}$ and α_{app} increases drastically after *f* > 0.5

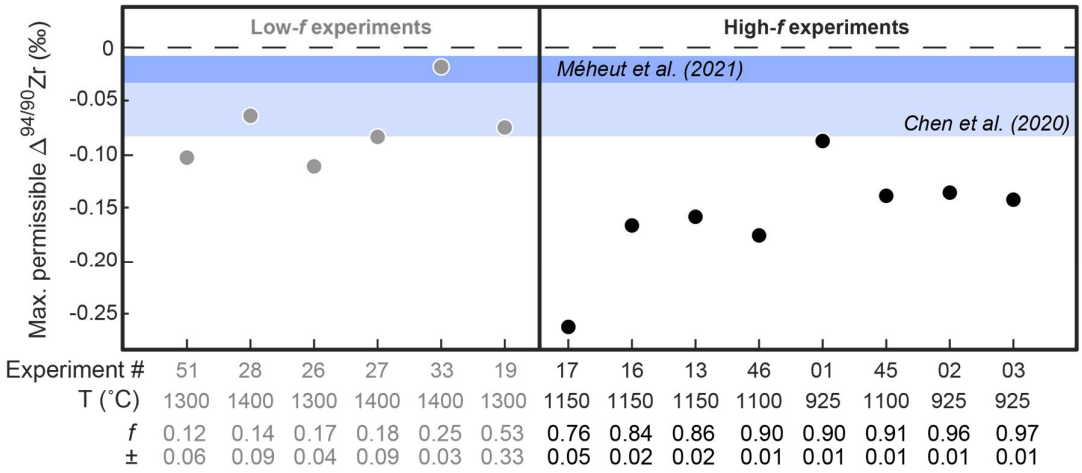

Figure S-4 Magnitude of α_{app}, the maximum permissible value for the effective $\alpha_{zircon\text{-}melt}$ governing each experiment, as a function of f for all our experimental products. Note that larger magnitudes of α_{app} for high-f experiments are expected, given the strong dependence of α_{app} with f for Rayleigh systems with $f > 0.5$ (Fig. S3b).

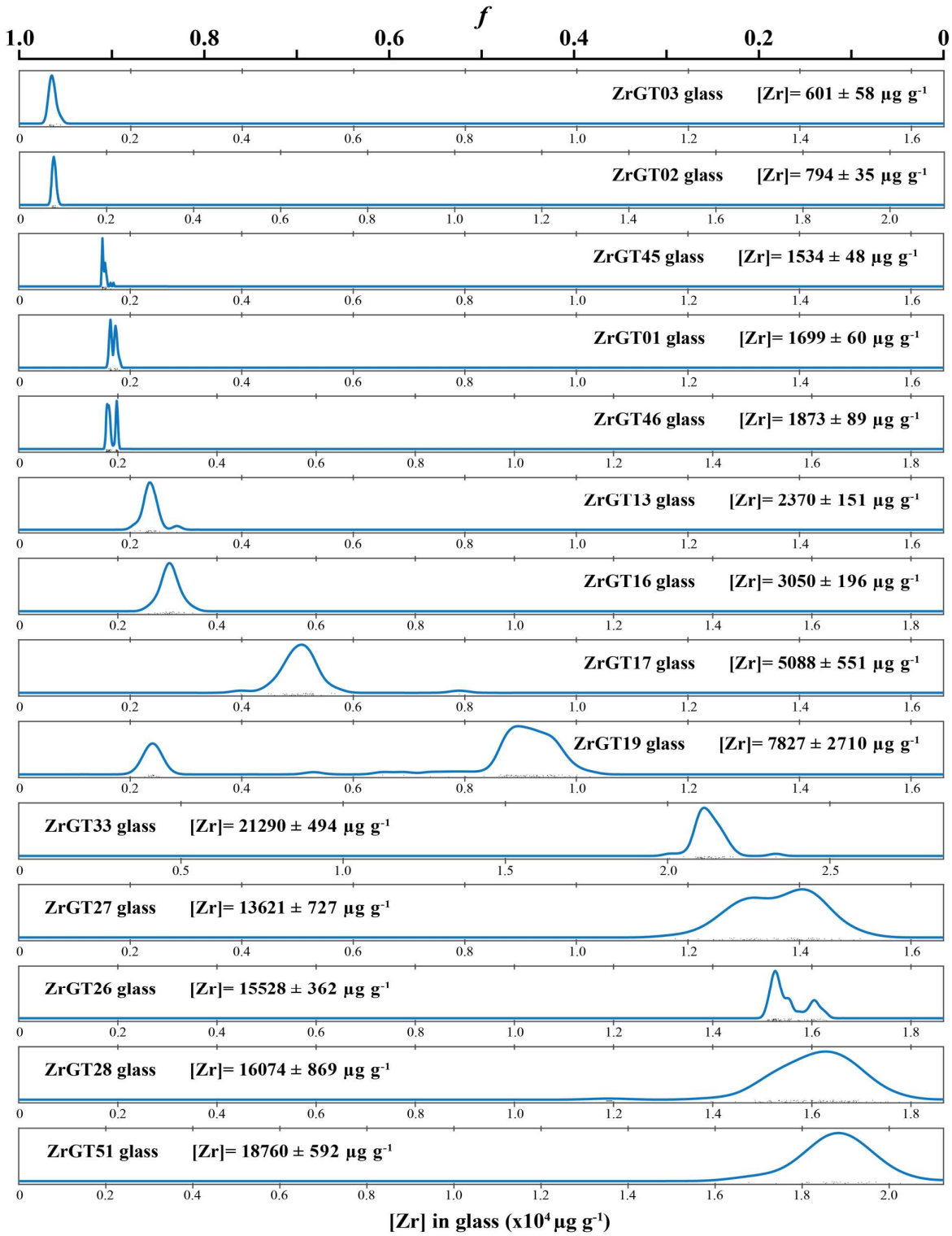

Figure S-5 Kernel probability density estimates showing the spatial variability of Zr concentration values (bottom axis) and *f* values (top axis) within the glass in each experiment, calculated using n= 20–90 single-spot SIMS measurements in glass fragments.

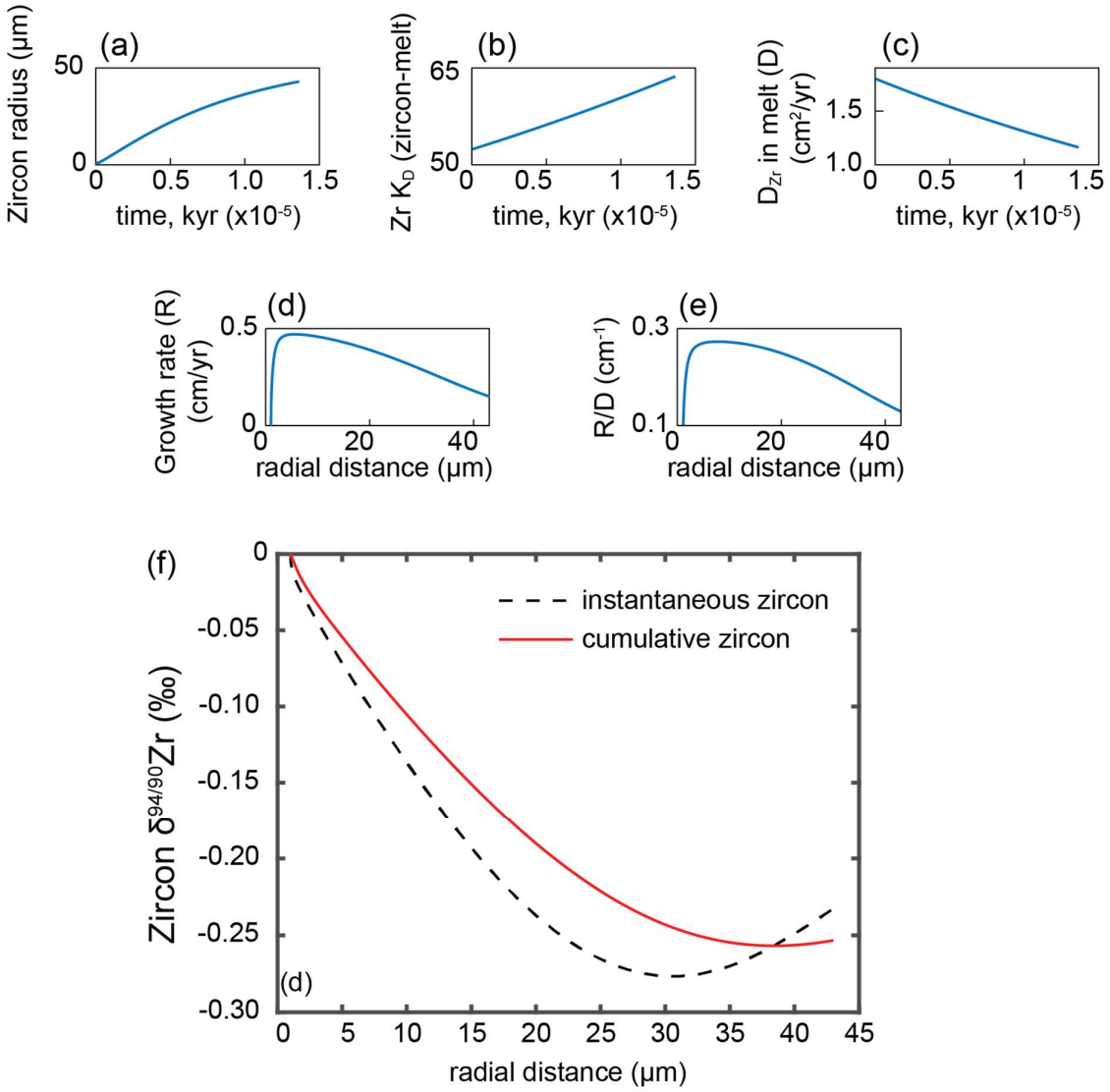

Figure S-6 Results of kinetic Zr isotope fractionation numerical model, performed using the code of Bindeman and Melnik (2022) using parameters described in the supplementary text. Outputs shown are: a) zircon radius (µm) *vs*. time (kyr x 10^{-5}); b) Zircon-melt Zr partition coefficient (K_D) *vs*. time (kyr x 10^{-5}); c) Zr diffusivity in the melt (D; cm^2/yr) *vs*. time (kyr x 10^{-5}); d) zircon growth rate (R; cm/yr) *vs*. crystal radial distance (µm); e) radial velocity of grain boundary migration over Zr diffusivity in the melt (R/D; cm^{-1}) *vs*. crystal radial distance (µm); and f) cumulative (solid red line) and instantaneous (dashed black line) zircon $\delta^{94/90}$Zr values *vs*. crystal radial distance. Results shown in Figure 3 are depicted as the 1000ln(α) *vs*. 10^6/T (K) relation of this model output for the cumulative zircon composition.

Supplementary Information References

Bindeman, I.N. and Melnik, O.E. (2022) The rises and falls of zirconium isotopes during zircon crystallisation. *Geochemical Perspectives Letters* 24, 17–21. https://doi.org/10.7185/geochemlet.2241

Botev, Z.I., Grotowski, J.F. and Kroese, D.P. (2010) Kernel density estimation via diffusion. The *Annals of Statistics* 38, 2916–2957. https://doi.org/10.1214/10-AOS799

Boehnke, P., Watson, E.B., Trail, D., Harrison, T.M. and Schmitt, A.K. (2013) Zircon saturation re-revisited. *Chemical Geology* 351, 324–334. https://doi.org/10.1016/j.chemgeo.2013.05.028

Chen, X., Wang, W., Zhang, Z., Nie, N.X. and Dauphas, N. (2020) Evidence from Ab Initio and Transport Modeling for Diffusion-Driven Zirconium Isotopic Fractionation in Igneous Rocks. *ACS Earth and Space Chemistry* 4, 1572–1595. https://doi.org/10.1021/acsearthspacechem.0c00146

Criss, R.E. (1999) Principles of Stable Isotope Distribution. Oxford Univ Press, New York. https://doi.org/10.1093/oso/9780195117752.001.0001

Guo, J.L., Wang, Z., Zhang, W., Ducea, M.N. (2020) Significant Zr isotope variations in single zircon grains recording magma evolution history. *Proceedings of the National Academy of Sciences* 117, 21125–21131. https://doi.org/10.1073/pnas.2002053117

Klaver, M., Ibañez-Mejia, M., Tissot, F. L. H., Vroon, P. Z. and Millet, M.-A. (2021) Reliability of detrital marine sediments as proxy for continental crust composition: The effects of hydrodynamic sorting on Ti and Zr isotope systematics. *Geochimica et Cosmochimica Acta* 310, 221–239. https://doi.org/10.1016/j.gca.2021.05.030

Méheut, M., Ibañez-Mejia, M., and Tissot, F.L.H. (2021) Drivers of zirconium isotope fractionation in Zr-bearing phases and melts: The roles of vibrational, nuclear field shift and diffusive effects. *Geochimica et Cosmochimica Acta 292*, 217–234. https://doi.org/10.1016/j.gca.2020.09.028

Pourmand, A., and Dauphas, N. (2010) Distribution coefficients of 60 elements on TODGA resin: Application to Ca, Lu, Hf, U and Th isotope geochemistry. *Talanta 81*, 741–753. https://doi.org/10.1016/j.talanta.2010.01.008

Pullen, A., Ibañez-Mejia, M., Gehrels, G.E., Ibáñez-Mejía, J.C. and Pecha, M. (2014) What happens when n= 1000? Creating large-n geochronological datasets with LA-ICP-MS for geologic investigations. *Journal of Analytical Atomic Spectrometry* 29, 971. https://doi.org/10.1039/C4JA00024B

Thomas, J.B., Bodnar, R.J., Shimizu, N., and Sinha, A. K. (2002) Determination of zircon/melt trace element partition coefficients from SIMS analysis of melt inclusions in zircon. Geochimica et Cosmochimica Acta, 66, 2887-2901. https://doi.org/10.1016/S0016-7037(02)00881-5

Tissot, F.L.H., Ibañez-Mejia, M., Vocke, R., Rabb, S., Fehr, M., Schönbächler, M., Tang, H., Young, E. (2022) Establishing and calibrating the Zr isotope Reference Material (iRM). Goldschmidt abstract 9653, Hawaii, US. https://doi.org/10.46427/gold2022.9653

Tompkins, H.G.D., Zieman, L.J., Ibañez-Mejia, M., and Tissot, F.L.H. (2020) Zirconium stable isotope analysis of zircon by MC-ICP-MS: Methods and application to evaluating intra-crystalline zonation in a zircon megacryst. *Journal of Analytical Atomic Spectrometry 35*, 1167–1186. https://doi.org/10.1039/C9JA00315K

Wang, Y., and Trail, D. (2019) Aluminum partitioning between zircon and haplogranitic melts: The influence of temperature and melt composition. *Chemical Geology 511*, 71–80. https://doi.org/10.1016/j.chemgeo.2019.02.016

Watkins, J.M., DePaolo, D.J. and Watson, E.B. (2017) Kinetic Fractionation of Non-Traditional Stable Isotopes by Diffusion and Crystal Growth Reactions. *Reviews in Mineralogy and Geochemistry* 82, 85–125. https://doi.org/10.2138/rmg.2017.82.4

Watson, E.B. and Müller, T. (2009) Non-equilibrium isotopic and elemental fractionation during diffusion-controlled crystal growth under static and dynamic conditions. *Chemical Geology* 267, 111–124. https://doi.org/10.1016/j.chemgeo.2008.10.036

Young, E.D. Manning, C.E., Schauble, E.A., Shahar, A., Macris, C.A., Lazar, C., and Jordan, M. (2015) High-temperature equilibrium isotope fractionation of non-traditional stable isotopes: Experiments, theory, and applications. *Chemical Geology* 395, 176–195. https://doi.org/10.1016/j.chemgeo.2014.12.013